ATAD3A has a scaffolding role regulating mitochondria inner membrane structure and protein assembly

Tania Arguello[1,4], **Susana Peralta**[1,4], **Hana Antonicka**[3], **Gabriel Gaidosh**[2], **Francisca Diaz**[1], **Ya-Ting Tu**[1], **Sofia Garcia**[1], **Ramin Shiekhattar**[2], **Antonio Barrientos**[1], **Carlos T. Moraes**[1,4,5,*]

[1]Department of Neurology, University of Miami Miller School of Medicine, Miami, FL 33136, USA

[2]Department of Human Genetics, Sylvester Comprehensive Cancer Center, University of Miami Miller School of Medicine, Miami, FL 33136, USA

[3]Department of Human Genetics and Montreal Neurological Institute, McGill University, Montreal, QC H3A 0C7, Canada

[4]These authors contributed equally to this work

[5]Lead contact

SUMMARY

The ATPase Family AAA Domain Containing 3A (ATAD3A), is a mitochondrial inner membrane protein conserved in metazoans. ATAD3A has been associated with several mitochondrial functions, including nucleoid organization, cholesterol metabolism, and mitochondrial translation. To address its primary role, we generated a neuronal-specific conditional knockout (*Atad3* nKO) mouse model, which developed a severe encephalopathy by 5 months of age. Pre-symptomatic mice showed aberrant mitochondrial cristae morphogenesis in the cortex as early as 2 months. Using a multi-omics approach in the CNS of 2-to-3-month-old mice, we found early alterations in the organelle membrane structure. We also show that human ATAD3A associates with different components of the inner membrane, including OXPHOS complex I, Letm1, and prohibitin complexes. Stochastic Optical Reconstruction Microscopy (STORM) shows that ATAD3A is regularly distributed along the inner mitochondrial membrane, suggesting a critical structural role in inner mitochondrial membrane and its organization, most likely in an ATPase-dependent manner.

Graphical abstract

In brief

Arguello et al. show that deletion of the mitochondrial protein ATAD3 in neurons leads to neuronal loss and death. The earliest phenotype is disruption of the mitochondrial inner membrane structure; OXPHOS complexes are affected later. ATAD3 is regularly spaced and has several interactors at the inner membrane, including CI subunits.

INTRODUCTION

AAA domain-containing protein 3 member A (ATAD3A) is a mitochondrial membrane protein from the family of ATPases associated with diverse cellular activities (AAA+), conserved in metazoans. *ATAD3A* gene absence results in embryonic lethality in flies (Gilquin et al., 2010), worms (Hoffmann et al., 2009) and mice (Goller et al., 2013; Peralta et al., 2018). In humans, *ATAD3* has been duplicated twice to form an array of three paralog genes organized in tandem (*ATAD3A, ATAD3B*, and *ATAD3C*), whereas other species, such as mouse, harbor only one gene. Disease-causing mutations in *ATAD3A* include duplications and deletions among different ATAD3 paralogs (Desai et al., 2017; Harel et al., 2016; Gunning et al., 2020; Frazier et al., 2021) and point mutations in the highly expressed *ATAD3A* gene (Cooper et al., 2017; Peralta et al., 2019; Dorison et al., 2020). Mutations in the ATAD3A gene have been associated with different neurodevelopmental disorders (Harel et al., 2016; Cooper et al., 2017) with clinical symptoms that include, among others,

global developmental delay, hypotonia, cardiomyopathy, congenital cataract, and cerebellar atrophy. ATAD3A has been considered one of the five most common genes associated with mitochondrial diseases in childhood (Frazier et al., 2021).

Within mitochondria, ATAD3A has been described as spanning both mitochondrial membranes with its C terminus facing the matrix and the N-terminal region located in the outer membrane (Gilquin et al., 2010; Baudier, 2018; Hubstenberger et al., 2010). As a member of the AAA+ ATPase family, ATAD3A is predicted to form hexameric ring structures at the C-terminal where the AAA+ ATPase domain is located. Functionally, ATAD3A has been associated with an array of roles within mitochondria, including membrane organization, mtDNA nucleoid organization, mitochondrial translation, cholesterol trafficking, and lipid metabolism, among others (van den Ecker et al., 2015; Fang et al., 2010; Lang et al., 2020; Jin et al., 2018; Peralta et al., 2018). However, the primary role of the protein remains unknown.

In this study, we generated a neuron-specific conditional knockout (nKO) *Atad3* mouse model and defined the molecular alterations occurring during the pre-symptomatic period to gain insight into the mechanisms leading to neuronal demise and neurological symptoms, which are overtly manifested 5 months after birth. To have a comprehensive view of the role ATAD3A plays in mitochondria, we used unbiased, integrated Omics, and high-resolution microscopy to identify the primary role of ATAD3. We have concluded that by evenly distributing across the mitochondrial network, and physically connecting the outer and inner mitochondrial membranes, ATAD3 sets a scaffolding platform and plays a prominent structural role in organizing protein complexes in the inner mitochondrial membrane.

RESULTS

Neuron-specific *Atad3* conditional knockout (*Atad3* nKO) mice showed reduced survival and impaired motor coordination with an onset at 5 months of age

We have created and characterized a neuron-specific *Atad3* conditional knockout mouse model (*Atad3* nKO). We crossed Atad3 floxed mice to mice expressing Cre recombinase under the calcium/calmodulin-dependent protein kinase II (CaMKIIα) promoter (Figures S1A and S1B). The CaMKIIα gene is expressed predominantly in the cortex and hippocampus neurons (Dragatsis and Zeitlin, 2000). Its expression starts at embryonic day E18.5 and reaches full activity by postnatal day p60. *Atad3*$^{F/F}$-CaMKIIα-Cre$^{+/-}$ mice, heretofore referred to as *Atad3* nKO were used as experimental animals and were compared to a control group (*Atad3*$^{F/F}$-CaMKIIα-Cre$^{-/-}$ or Atad3$^{F/W}$-CaMKIIα-Cre$^{-/-}$; Fig.S1B). The mice were genotyped as illustrated in Figure S1C, and the excision of exon 2 was confirmed by PCR (Figures S1D and S1E). The lack of ATAD3 was confirmed at the protein level by western blot analysis of cortical mitochondrial extracts (Figure 1A). *Atad3* nKO mice were born at Mendelian ratio and in both males (Figure 1B) and females (Figure S2A), *Atad3* nKO mice weighed less than the controls littermates. Despite being smaller, *Atad3* nKO animals gained weight at similar rates compared to controls until the age of 3 months in males (Figure 1B) and 4 months in females (Figure S2A), when they started to lose body weight. Five months old *Atad3* nKO mice presented with a marked kyphosis (Figure 1C), a

sign of neurodegeneration (Thomas et al., 2006). Fifty percent of the *Atad3* nKO mice died before 6 months of age (Figure 1D).

Atad3 nKO mice at 3 and 4 months of age showed normal nocturnal locomotor activity (active period). Starting at 5 months of age, they showed increased nocturnal locomotor activity (Figure S2; Video S1). During the day, *Atad3* nKO mice 5 months and older presented catatonic episodes (Video S2). Motor coordination measured by rotarod was normal for 3- and 4-month-old *Atad3* nKO mice (Figure 1E). However, at 5 months of age *Atad3* nKO mice showed a lower rotarod performance, and by 6 months, *Atad3* nKO mice could not perform the task (Figure 1E). Moreover, normal exploratory activity measured in the open field showed increased ambulatory time for the *Atad3* nKO (Figure S2). Most 4–5-month-old *Atad3* nKO mice tested showed a strong limb clasping (a sign of neurodegeneration; Johnson et al., 2013; Maltecca et al., 2015) phenotype (Figures 1F and 1G). By 6 months of age, *Atad3* nKO mice were severely hunched, very sick, and with untidy appearance because they ceased grooming (Fig.S2). According to animal guidelines, they were sacrificed at 6–7 months for tissue analyses.

These results showed that the ablation of Atad3 in neurons impaired motor coordination and disrupted the stereotypical rodent behavior, with an onset at 5 months of age.

Lack of ATAD3 in neurons disrupts mitochondrial cristae structure causing a decrease in mitochondrial size and neuron cell death

Brain isolated from *Atad3* nKO mice showed a gradual decrease in size from the age of 5 months that worsened with time (Figures 2A and S3). The loss of motor cortex mass was noticeable in *Atad3* nKO mice 7 months old after dissection and before observing the samples under the microscope (Figure S3A). The relative brain weight/body weight was not changed since there was a decrease in body weight in *Atad3* nKO mice (Figures S3B and S3C).

Hematoxylin and Eosin staining of the brains did not show apparent anatomical alterations in mice 3 months old (Figure S3D). However, cortex and hippocampal regions were smaller in *Atad3* nKO mice 5 months old (Figure 2B). These differences worsened with time (see *Atad3* nKO mice 7 months old, Figure S3F).

To test whether ATAD3 depletion resulted in neuronal cell death, we analyzed a neuronal marker (TUJ1) in the cortex by western blots. At 3 months of age TUJ1 protein levels were normal in *Atad3* nKO males (Figure 2C). However, we found a 50% reduction in TUJ1 protein at 5 months of age in *Atad3* nKO males, indicating neuronal loss.

Transmission electron microscopy (TEM) images from hippocampus CA 1 region showed mitochondrial inner membrane alterations in the hippocampus region of pre-symptomatic nKO mice 2 months old (Figure 2D). Quantification of mitochondria showed that size (perimeter and area), as well as cristae structure (per perimeter and mitochondrial area), were significantly reduced in *Atad3* nKO mice (Figure 2E). Defective mitochondria were characterized by increased matrix space. Cristae was markedly reduced and appeared detached from the inner mitochondrial boundary forming instead "vesicle-like" structures

inside the matrix space. Ultrastructural analysis of the hippocampus of 5-month-old *Atad3* nKO mice also showed mitochondria with reduced size and with abnormal cristae (Figure S4). In addition, we observed an accumulation of large lipid droplets in the brain of 5-month-old *Atad3* nKO mice that were absent in the preparations from control mice (Figure S4).

The reduced mitochondrial size observed in the brains of *Atad3* nKO suggested reduced mitochondrial mass. To test this possibility, we quantified relative mtDNA levels by real-time PCR of total DNA isolated from cortex and hippocampus from 3- and 5-month-old male mice. Whereas at 3 months of age, the mtDNA levels were similar in nKO and control tissues, we detected a significant decrease in nKO cortical and hippocampal mtDNA at 5 months of age (Figure 2F).

These results indicated that the lack of ATAD3 in neurons induced neurodegeneration in mice progressing from early inner membrane/cristae abnormalities, followed, months later, by mtDNA depletion and ultimately cell death. mtDNA depletion, signs of neurodegeneration, and the onset of the motor phenotypes were observed only at 5 months of age.

Lack of Atad3 expression is associated with isolated Complex V assembly deficiency in pre-symptomatic mice

In 3-month-old male mice, we did not detect changes in the steady-state levels of the individual OXPHOS complex subunits tested, including NDUFB8 (complex I), COX1 (complex IV), and SDHA (complex II) (Figures 3A-3C). In contrast, the levels of most mitochondrial markers were reduced in 5-month-old male mice (Figure 3B). Blue Native PAGE analysis of mitochondrial samples prepared in the presence of digitonin (1:8 protein to detergent ratio) showed a decrease in the assembled F_1-F_o ATPase synthase (Complex V) in the hippocampus of 3-month-old male mice, whereas other complexes remained unchanged (Figure 3E). These results indicate that the isolated complex V abnormalities precede any neuronal damage and define the pre-symptomatic stage of *Atad3* nKO. The structure of the IMM is important to the stability of OXPHOS complexes, including complex V, which promotes curving of the IMM by dimerization (Kühlbrandt, 2019).

The levels of assembled complexes containing mtDNA-encoded subunits, such as complex I, III, IV, and V were decreased in 5-month-old *Atad3* nKO male mice, whereas the exclusively nucleus-encoded complex II remained unchanged (Figures 3F and 3H). This result agrees with the mtDNA depletion detected in the cortex and hippocampus of 5-month-old *Atad3* nKO male mice (Figure 2F).

Carnitine and Linoleic Diacylglycerol pathways were altered in *Atad3* nKO brains

We performed multi-omics analyses in *Atad3* nKO male mice between 2 and 3 months of age before the disease onset (Figure 4A). This approach included RNA-seq, metabolomics, and lipidomic analysis in the motor cortex homogenates (Figure 4A). Our transcriptomics analysis identified ATAD3A as the main decreased transcript in the KO group (fold change = −1.0) along with 22 additional differentially expressed genes (Figure 4B). Among the most significantly changed transcripts was the mitoribosome large subunit gene, MRPL12

(fold change = −0.85), which has both roles in mitochondrial biogenesis and a second function in activating mitochondrial transcription (Surovtseva et al., 2011; Figure 4B-C). Functional enrichment annotation identified transcripts associated with neuronal vesicle transport, migration processes, mitochondrial chaperone regulation as well as cytoplasmic RNA and ribosomal regulation (Table S1). These findings point to an early neuronal stress response in the motor cortex, including an initial stress in mitochondria-related functions.

Metabolomics analysis initially detected a total of 503 unique metabolites among the control and *Atad3* nKO male cortex samples. Partial Least Square Discriminant Analysis (PLS-DA) revealed a clear separation of groups already in the two first principal components (1 = 60.9%, 2 = 23%, and 3 = 2.7%), indicating a significant change of metabolite profiles between *Atad3* nKO mice and control littermates (Figure 4D). Analysis of differential expression using Significance Analysis of Microarrays (SAM) identified 27 altered metabolites, all of which were increased in the *Atad3* nKO motor cortex group relative to the control group (delta = 1.4). Enrichment analysis of these metabolite sets grouped most candidates into two main pathways related to transport across mitochondrial membranes (Figure 4E). One set included carnitine and acylcarnitine metabolites from the carnitine pathway, involved in the transport of activated long fatty acyl chain through the mitochondria membrane. The second set included several linoleic diacylglycerol (DAG) forms (oleoyl (18:1), palmitoyl (16:0), and stearoyl (18:0) linoleoyl-glycerol (18:2)), which are precursors of the cardiolipin synthesis pathway, the main fatty acyl moiety in mitochondria.

Global lipidomics profiling of the cortex of the *Atad3* nKO mice disclosed a decrease of total phosphatidylcholine (PC) (Figure 4F). PC is one of the most abundant phospholipids in both mitochondrial membranes, and the major linoleic acid donor during cardiolipin synthesis and remodeling (Fajardo et al., 2017; Chicco and Sparagna, 2007). We then performed a focused cardiolipin content profiling that showed a total cardiolipin decrease in *Atad3* nKO cortex (Figure 4F).

Overall, our integrated multi-omics analysis suggested an early disruption of metabolic processes involved in mitochondrial lipid membrane architecture and transport of fatty acids through the mitochondrial membrane in the absence of ATAD3, linking the accumulation of linoleic DAG precursors and decreased PC (Figure 4G).

ATAD3A interacts with multiple mitochondrial protein complexes fundamental for membrane integrity

To further gain insight into the functional role of the ATAD3 protein, we extended our studies to cell culture models. We next looked for interactors of ATAD3 by coimmunoprecipitation (coIP) and mass spectrometry (MS) and detected 280 interactors in human HEK293T cells. Using the top 100 hits for gene set enrichment analysis, we identified several members of complex I mitochondrial assembly, mitochondrial membrane quality and membrane organization machinery (Figure 5A). Enrichment analysis included association with the prohibitin complex (PHB, PHB2, DNAJC19, STOML2,) AAA+ *m*-proteases (YME1L) and *i*-proteases (AFG3L2, SPG7), MICOS complex protein members (IMMT, CHCHD3), cristae remodeling OPA1, LETM1, and F_1-F_o ATP synthase complex

(ATP5O, ATP5L), supporting the role of ATAD3 in mitochondria cristae and inner membrane structure/organization.

ATAD3A has a conserved ATPase domain located in the C-terminal region of the protein, which contains canonical residues responsible for the ATP catalytic activity. This domain has two Walker motifs (Walker A and B), and a Second Region of Homology (SRH) motif. The Walker A and Walker B motifs are responsible for the binding and hydrolysis of ATP, respectively (Hanson and Whiteheart, 2005). To identify the potential candidates that could interact with the ATPase domain or depend on ATP binding, we generated a mutation in the conserved Walker A motif: a change of glycine (G) to aspartate (D) in position 355 (Figure 5B) (within motif GXXXXGK[T/S]-where X can be any amino acid). The ATAD3 mutation (p.G355D) is associated with hereditary spastic paraplegia (HSP) in humans (Cooper et al., 2017) and is predicted to eliminate the substrate binding affinity resulting in the complete inactivation of the AAA protein.

We used the proximity-dependent biotinylation assay (BioID) approach to map proximity interactors to the ATAD3A C-terminal region of both wild-type and G355D mutant *in vivo*. Mass spec analysis revealed a list of 128 and 133 high-confidence proximity interactors (for the wild-type ATAD3A and G355D mutant baits, respectively) (Figure 5C). The 103 interactors were common among wild-type ATAD3A and the G355D mutant, suggesting that the G355D change in the binding pocket of the ATPase domain has little or no effect over these interactions. Among the common interactors, we confidently identify ATAD3B and ATAD3A (Figure 5D), which were previously found to interact (Merle et al., 2012). In addition, enrichment analysis identified other inner membrane components, including members of the mitochondrial complex I, mitoribosome, and fatty acid metabolism (Figure 5E). Interestingly, 25 proteins, including assembly factors of complex I or mitoribosome subunits were identified as prey exclusively when there was an intact and functional ATPase domain as bait, indicating that their interaction relies on the ATPase nucleotide-binding region and could be mediated by the ATPase catalytic activity. We also identified 30 other candidate preys associated only with the G355D mutant bait (Table S2), among these ADP/ATP carriers SLC25A5 and SLC25A6, as well as SLC25A10, a dicarboxylate carrier which has been shown to play a role in *de novo* fatty acid synthesis (Mizuarai et al., 2005).

ATAD3A interacts with LETM1

When proteins identified by both the co-immunoprecipitation and BioID approaches are compared, 14 common proteins emerge, with LETM1, a regulator of mitochondrial morphology and cristae structure and mitochondrial proton/cation exchanger protein, among the highest ranked hits (Figure 5F).

LETM1 is an inner mitochondria membrane protein with the N-terminal domain facing the inter-membrane space and the C-terminal domain carrying two EF-hand domains extruding toward the matrix. Using an *in vivo* protein fragment complementation assay (NanoBiT, Promega), we tested both interaction orientations (N and C-terminal regions) between LETM1 and the matrix-facing C-terminal of the ATAD3A protein. Mitochondrial localization was confirmed by immunofluorescence using antibodies for mitochondria (TIM23) and large Bit (LgBit) subunit of the fused ATAD3A. The NanoBiT assay in

HEK293T showed a stronger interaction between the ATAD3 C-terminal region (ATAD3$_{(C)}$) and the C-terminal of LETM1 (LETM1$_{(C)}$) when compared to the N-terminal region of LETM1 (LETM1$_{(N)}$ (Figure 5G). LETM1 was a top interactor in ATAD3A of both wild-type and G355D-mutated ATPase domain in HEK293T cells (Figure 5C), suggesting that the interaction between these proteins does not rely on the AAA+ domain binding function within the Walker A motif.

Complexome data mining shows ATAD3′s dependence on cardiolipin to fractionate as a large complex

We further explored the interactions identified in additional available databases. We mined a co-fractionation mass spectrometry (CF-MS) database created by the Foster Lab, which included a total of 206 CF-MS experiments (Skinnider and Foster, 2021). Although the web interface allows to input different proteins and analyze their interactions based on CF-MS, it is limited by the presence of all the desired proteins in the database. We entered ATAD3A, PHB, PHB2, LETM1, TFAM, the m-AAA-proteases (AFG3L2, SPG7), and MRPL12 and found interactomes in mouse samples. ATAD3, PHB, PHB2, LETM1, AFG3L2, and SPG7 have a large number of interactions, either directly or through complex I subunits (Figure S5A). In contrast, TFAM or a mitoribosome representative (MRPS12) did not (Figure S5B).

Another database of interest was published by the Huynen Lab and included CF-MS of fibroblast samples of four patients with Barth syndrome, which have different mutations in the Tafazzin gene (Van Strien et al., 2019). Tafazzin gene product (TAZ1) remodels newly synthesized cardiolipin (CL), functioning as a monolysocardiolipin (MLCL) transacylase. In the absence of an active TAZ1, no mature CL is formed (Xu et al., 2006). Because CL has a major role in inner mitochondrial membrane organization, we mined their data for changes in ATAD3A complex arrangements. The data showed that ATAD3A fractionated as a very high molecular weight complex in controls, whereas all TAZ1 mutants showed ATAD3A migrating at a much smaller size (Figure S5C). Marked changes were also observed for LETM1 and AFG3L2 (Figure S5C). When analyzing control samples, we found ATAD3A co-fractionating with AFG3L2, PHB, and even with complex I. However, LETM1 showed only a small fraction at this high molecular weight, suggesting a potentially dynamic/weak interaction. PHB and PHB2 steady-state levels were previously reported to be increased in TAZ1 mutants (Van Strien et al., 2019). Another CF-MS study (Stepanova et al., 2019), performed in neonate brain mitochondria under normal and succinate-supplemented conditions (which promotes reverse electron transfer/ROS formation), showed that only a small fraction of ATAD3 and LETM1 fractionate as a very large complex in either condition (Figures S5D and S5E).

A Bio-ID database focused on human mitochondrial proteins found that ATAD3A and ATAD3B were frequent proximity interactors for IM or intermembrane space proteins, possibly due to their abundance and role in organizing complexes in the inner mitochondrial membrane (Antonicka et al., 2020). One bait, MTCH1, exhibited increased proximity interaction with ATAD3A as compared to the other baits in the dataset. MTCH1 is an outer membrane carrier protein of unknown function (Nelo-Bazán et al., 2016) which may interact with the outer membrane segment of ATAD3 in a more stable manner.

ATAD3A in HeLa cells is regularly distributed along the mitochondrial membrane

ATAD3A has a complex topology that spans both mitochondrial membranes, with the N-terminal domain facing the outer membrane and the C-terminal domain facing the matrix. To understand the nanoscale membrane architecture organization of the endogenous ATAD3A and its contribution to the mitochondrial membrane organization, we used STORM (Stochastic Optical Reconstruction Microscopy) imaging of mitochondria in human HeLa cells (Rust et al., 2006).

We visualized the N-terminal domain of ATAD3A in association with mitochondrial markers located in the outer (TOM20) and inner (TIM23) mitochondrial membranes (Figure 6A). Using an antibody recognizing the N terminus of ATAD3 at a resolution of 50 nm, we found ATAD3A, TOM20, and TIM23 to have a high degree of co-occurrence (measured as Mander's coefficient $M_{(A)}$). The signals for TIM23 and TOM20 were distributed along the mitochondrial network. TOM20 showed a characteristic cluster appearance similar to what was already described at the nanolevel resolution (Wurm et al., 2011), whereas the ATAD3A signal appeared less abundant but distributed at more regular intervals along the mitochondrial branches (Figures 6A and 6B).

We also evaluated the spatial submitochondrial localization of the mtDNA with the N-terminal region of the ATAD3A protein (Figure 6C), as ATAD3A has been associated with mitochondrial nucleoids (He et al., 2012). We did find higher co-occurrence values of the mtDNA signal with ATAD3A signal ($M_{(A)}$), which confirms their interaction but also showed that ATAD3A foci are more abundant than mtDNA, reflected by a lower Mander's B coefficient ($M_{(B)}$) (Figure 6D). This indicates that most mtDNA is associated with ATAD3A, but not all ATAD3A foci are associated with the mtDNA nucleoids, suggesting a possible compartmentalization of tasks for ATAD3A molecules.

Upon closer examination of the ATAD3A signal, STORM images revealed a remarkably regular pattern of ATAD3A distribution along the mitochondrial membranes. To detect any periodicity in the ATAD3A signal, we did employ Fast Fourier transformation (FFT) analysis of 560 different signal tracings of the reconstructed STORM images using the ATAD3 N-terminal antibody. FFT detected several frequency peaks corresponding to periodic wave signals above the amplitude threshold (50% of the maximum peak signal detected per trace; Figure 6E) which correspond most likely to the distribution of the ATAD3A among different mitochondria sizes within the cell. Histogram distribution of the total detected periods showed that ATAD3A signal is distributed preferentially between 0.5 to 1.0 μm (best Gaussian fit: Amplitude:526.3, mean:0.8461, SD:0.4339). These results demonstrate that ATAD3A is periodically interspersed within the mitochondria, consistent with the hypothesis that ATAD3A provides a structural/organizational role to the mitochondrial membranes.

ATAD3A forms homoclusters at the N- and C-terminal domains

Members of the AAA+ ATPase family are known to form hexameric ring complexes and organize into homodomains or heterodomains with the proteins of the same family (Miller and Enemark, 2016). ATAD3A has been shown to oligomerize and has been

detected in several high molecular weight complexes by Blue Native PAGE (Goller et al., 2013;Frazier et al., 2021; Peralta et al., 2018). ATAD3A is also predicted to form hexameric structures at the C-terminal region where the AAA+ ATPase domain is located. However, high spatial resolution analysis of ATAD3A oligomers is lacking. We evaluated the protein's ability to form oligomers at the nanoscale resolution taking advantage of the single-molecule localization microscopy (SMLM). Using SR-Tessler, a Voronoi tessellation analysis technique that measures clusters at the SMLM resolution, and antibodies against epitopes located in the N-terminal and C-terminal region of the ATAD3 protein, we did find that ATAD3A form organized clusters using either antibody (Figure 6F). The quantification of the ATAD3A clusters using parameters described in methods identified clusters with mean diameters of 110.7 nm (95% CI = 108.4-113) at the N-terminal region and 139.0 nm (95% CI = 136.1-142) at the C-terminal region. These results suggest that ATAD3A clusters form a central channel as many other members of the same AAA+ ATPase family (Gates and Martin, 2020). We also tested if the clusters observed were homo-oligomers composed only of ATAD3A molecules or hetero-oligomers containing ATAD3A and ATAD3B proteins. Using an antibody recognizing only ATAD3B and the same cluster threshold parameters, we did not observe organized clusters, whereas the ATAD3A cluster size was maintained at around 125 nm (Figure 6G). This indicated that the identified clusters of the endogenous ATAD3A are homodomains consisting preferentially of ATAD3A molecules.

DISCUSSION

ATAD3A has been associated with several important roles inside mitochondria; however, its primary function has been elusive. To investigate this question, we generated a brain conditional knockout mouse model and defined the pre-symptomatic stage to explore the molecular pathogenesis.

Although mitochondrial inner membrane abnormalities can be a consequence of several biochemical defects, *in toto*, our data, as well as the considerable number of previous studies (Gerhold et al., 2015; Peralta et al., 2018; Cooper et al., 2017; Gilquin et al., 2010; Dorison et al., 2020) suggest that ATAD3 has a major role in structurally organizing the mitochondrial membranes (Figure 6H). We found that ATAD3 depleted neurons from pre-symptomatic mice have disruptions of the mitochondrial membrane cristae and reduction of mitochondrial size as early as 2 months, before the onset of symptoms. This was followed by a decrease in complex V steady-state levels at 3 months. Complex V is responsible for the ATP synthesis during oxidative phosphorylation, but also has a critical role in shaping the inner mitochondrial membrane, stabilizing the cristae ultrastructure (Salewskij et al., 2020). Decreased levels of complex V in our model could be secondary to cristae disruption. These observations are in agreement with previous work by our group in a model of ATAD3 ablation in skeletal muscle (Peralta et al., 2018). Cristae morphology disorganization was the first detectable phenotype. Moreover, in the case of the muscle KO, complex V decrease was observed at 3 months, coinciding with the onset of the phenotype. Also supporting a role in scaffolding, Zhao et al. (2019) showed that mutant huntingtin interacts with ATAD3, promoting K135 deacetylation and interaction with Drp1, leading to mitochondrial fragmentation.

ATAD3 was previously shown to be enriched in ER-mitochondrial junctions termed mitochondria-associated membranes (MAMs) (Poston et al., 2013). In addition, ATAD3 participates in cholesterol transport in mitochondrial membranes (Gilquin et al., 2010), suggesting that ATAD3A is tethered to the cytosol and adjacent compartments such as ER (Issop et al., 2015; Baudier, 2018). We focused our protein-protein interaction at the inner mitochondrial membrane side, but a recent study found that the ATAD3A was captured as prey by 33 different baits (Antonicka et al., 2020) some of which localized to the OMM (8 baits), IMM (13 baits), or matrix (12 baits).

Our metabolomics analysis performed in *Atad3* nKO mice revealed several linoleic diacylglycerol precursor candidates accumulated in pre-symptomatic mice and a decrease in the total phosphatidylcholine (PC) profile (found by lipidomics) when compared to all the major phospholipids classes. Phosphatidylcholine is the most abundant structural phospholipid in mitochondria outer and inner membrane and one of the most important substrates during cardiolipin remodeling. Once cardiolipin is synthesized the novo, PC acts as a major donor of linoleic acyl groups to the mature cardiolipin (Mejia and Hatch, 2016). Total cardiolipin decrease content did not reach significance by ANOVA at this early time, but defects in ATAD3A could result in lower availability of cardiolipin precursors observed as an alteration of linoleic diacylglycerol and PC in our *Atad3* nKO model. Although these could contribute to cristae and mitochondrial membrane disruption observed by electron microscopy, they can also be consequences of a structurally compromised IMM. The mechanism of PC transport is not well understood (Vance, 2020). ATAD3A does not have predicted lipid-binding transfer domains and, in our high-resolution analysis, has a regular distribution across the mitochondrial membrane. These features do not fit with a proposed role as a dedicated mitochondria-ER tether protein (Scorrano et al., 2019), but they may interact during specific events (e.g., mitochondrial fission). We suggest that ATAD3 instead facilitates the transport of phospholipids across mitochondria membranes working in close vicinity to MAM proteins but not necessarily as an exclusive integral resident of the MAMs. ATAD3 could serve instead as a scaffold sorting or/and recruiting proteins required during the processing and distribution of lipids within the membranes in a dynamic and transient fashion.

Our metabolomics analysis performed in *Atad3* nKO mice at the pre-symptomatic stage also revealed altered pathways related to the transport of lipids along mitochondria membranes. The carnitine shuttle pathway, which transports long fatty acid chains through the mitochondrial inner membrane, was altered. Accumulation of carnitine and already activated acyl-carnitine metabolites (which result from the Coenzyme-A group (CoA) exchange to carnitine by the carnitine palmitoyltransferase 1 (CPT-I) enzyme (Houten et al., 2016), could also be associated with a disruption of the inner mitochondrial membrane structure.

The inner mitochondrial membrane organization is maintained by several protein complexes. Our IP data show that ATAD3A nanodomains associates with several members of the inner mitochondrial membrane and cristae organization complexes in the inner mitochondrial boundary suggesting that ATAD3A participates in the maintenance/organization of the inner mitochondrial membrane structure (Figure 6H). Interestingly, these members included the

Prohibitin complex, which in many ways resembles ATAD3 at the functional level. It has been proposed that the Prohibitin complex works as a "scaffold for proteins and lipids regulating mitochondrial metabolism, including bioenergetics, biogenesis, and dynamics in order to determine the cell fate, death or life" (Signorile et al., 2019). PHB1 and PHB2 are also mediators of cristae structure, remodeling through the association with other complexes (such as m-proteases or OPA1) (Osman et al., 2009; Signorile et al., 2019). Proteins re-distribute dynamically within the membranes so that several proteins may interact transiently with ATAD3A according to the physiological state or energetic demands of the cell.

When evaluating the ATPase domain activity located at the C-terminal region of ATAD3A, the BioID interactions revealed that most of the candidate proteins belong to complex I subunits and assembly factors, as well as mitoribosome and other inner membrane components. Although the effect of the mutation in the Walker A motif (p.G355D) did not have a major impact on the interaction of many of those candidate members, few mitoribosome large subunits, as well as complex I subunits were present exclusively when the Walker A binding motif of the ATAD3A was intact. This indicates that subunits of the complex I and mitoribosome candidate proteins rely on a functional ATPase activity for their interaction and suggest that ATAD3A and, more specifically, the AAA+ ATPase domain most likely participate in interacting with proteins that require ATPase hydrolysis potentially during processes like assembly or disassembly of complex I and mitoribosomes. One BioID interaction worth noting is the one with CI subunit NDUFS2. This interaction had twice the counts in the ATPase mutant, potentially because the ATPase activity may be required for ATAD3A to "release" this interaction.

Analysis of other top interactor candidates demonstrated that LETM1 interacts with ATAD3A in human cells. LETM1 is an inner mitochondrial membrane protein with a critical role in maintaining cristae morphology (Nakamura et al., 2020) and cation homeostasis (Austin and Nowikovsky, 2019; Lin and Stathopulos, 2019). We observed that LETM1 interacts through its C-terminal region to ATAD3 *in vivo*. Interestingly, the BioID results showed that LETM1 interaction was not abolished after mutating the Walker A domain of ATAD3A, indicating that LETM1-ATAD3A interaction is not dependent on the AAA domain function. LETM1 can oligomerize and form homodimers through a domain identified at the C-terminal region. This process is regulated by proteins from the AAA+ ATPase family resembling the mitochondrial chaperone BCS1L (Tamai et al., 2008). BCS1L, an assembly factor for OXPHOS complex III, was also found through BioID as prey of ATAD3A ATPase mutant, linking these candidates together. Additionally, the yeast homolog of LETM1, Mdm38, interacts with the ribosome and Oxa1 to facilitate membrane insertion of mitochondrial proteins (Bauerschmitt et al., 2010). It is important to emphasize that the overall data (ours and that from the literature) suggest a weak and dynamic interaction between ATAD3 and several IMM members. This is supported by complexome studies that show small fractions of ATAD3A associated with larger complexes. Cardiolipin is also critical for ATAD3 association as a large complex, as it dissociates into smaller MW fractions in tafazzin mutants.

STORM analysis revealed that ATAD3A is distributed regularly (spaced by 0.5-1 µm) along the mitochondria branches in very distinct clusters emphasizing the role of ATAD3A in

mitochondrial membrane architecture and likely being part of the mechanical structure within the mitochondria that contribute to their shape (Figure 6H).

We also demonstrated that ATAD3A showed oligomer-like features not only at the C-terminal where the AAA+ ATPase domain is located but also at the N-terminal region. The N-terminal domain has been shown to associate as a dimer, interact with the outer membrane, and is predicted to support oligomerization due to two coil-coil domains (Gilquin et al., 2010; Zhao et al., 2019). Although we were not able to quantify the number of molecules present in the ATAD3A oligomers, the N and C termini have a cluster size of approximately 110.7 nm and 139.0 nm, respectively, suggesting that ATAD3A could define a central channel to induce conformational changes on several protein substrates through cycles of ATP binding and hydrolysis like many of the AAA+ ATPase family members. Structures of AAA proteins (de la Peña et al., 2018; Gates et al., 2017; Puchades et al., 2019; Miller and Enemark, 2016) showed that typically, AAA proteins form an hexameric assembly and bind to their substrate in a central channel. ATP hydrolysis around the hexamer generates mechanical forces that pull the substrate in two amino acid steps through the channel. ATAD1 has adapted this mechanism to extract tail-anchored proteins from the mitochondrial outer membrane (Wang and Walter, 2020). We speculate that ATAD3 evolved a similar mechanism to arrange protein complexes in the mitochondrial inner membrane.

In conclusion, our study demonstrated that ATAD3A has a critical role in mitochondrial inner membrane structure maintenance. ATAD3Aforms homodomains at the N- and the C-terminal regions and is distributed in a periodic pattern along the mitochondrial network, which contributes to maintaining its structural morphology. Due to this spatial organization and major role in IMM integrity, we propose that ATAD3 plays an important role as a scaffold protein interacting with multiple protein substrates in an ATP-dependent manner, possibly helping coordinate the arrangement of protein complexes in the IMM and consequently affecting the function of many biological processes that take place at the IMM.

Limitations of study

The main limitation of this study is that the molecular mechanism of ATAD3 is still unknown. We propose that ATAD3 works as an IMM organizing/scaffold center based on the phenotypes and interactions observed, both in wild-type cells and conditional knockouts. Another limitation is that we were not able to produce knockouts in cultured cells, suggesting that ATAD3 function is essential for cell survival.

STAR★METHODS

RESOURCE AVAILABILITY

Lead contact—Further information and requests for resources and reagents should be directed to and will be fulfilled by the Lead Contact, Carlos Moraes (cmoraes@med.miami.edu).

Materials availability—Further information and requests for resources and reagents should be directed to and will be fulfilled by the lead contact.

Data and code availability

- RNA-seq and Metabolomics data have been deposited at GEO (GSE186409) and Metabolights (MTBLS3786) respectively and are publicly available as of the date of publication. Accession numbers are listed in the key resources table. All other data reported in this paper will be shared by the lead contact upon request. This paper analyzes existing, publicly available data. These accession number for the datasets are listed in the key resources table.

- This paper does not report original code.

- Any additional information required to reanalyze the data

reported in this paper is available from the lead contact upon request.

EXPERIMENTAL MODEL AND SUBJECT DETAIL

Creation of Atad3 nKO mice model—We acquired from the Knockout Mouse Project repository an embryonic stem cell clone where endogenous *Atad3* has been modified by homologous recombination (https://www.komp.org/), Figure S1A). We injected the embryonic stem (ES) cell line containing *Atad3* trap gene (clone CDS37385, derived from JM8.N4 cells, background 6N) into C57BL/6J derived blastocysts and the embryos achieved were implanted into pseudo pregnant foster mothers. The generation of chimeras and excision of the neomycin selection marker was previously described in (Peralta et al., 2018). To generate the *Atad3* neuronal-specific knockouts (*Atad3* nKO), homozygous *Atad3* *(LoxP/LoxP)*, were mated to double heterozygous mice *Atad3* *(+/LoxP)*, *CaMK-IIα* Cre *(+/−)*, and the resulting progeny with the desired genotype selected for phenotypic studies. All experiments and animal husbandry were performed according to a protocol approved by the University of Miami Institutional Animal Care and Use Committee. Mice were housed in a virus-antigen-free facility of the University of Miami, Division of Veterinary Resources in a 12-h light/dark cycle at room temperature and fed *ad libitum*. Females and Males mice were analyzed in this study. Animals were analyzed for survival experiment from birth until dead (7-8-month-old). Animal studies were performed mainly at 3 month, and 5 months in males or at 2.5-month-old as specified within the text for each experiment.

Sex and age/developmental stage of mice—We studied both males and females. The ages selected were based on the onset of phenotypes.

Mammalian cell culture—HEK293T and HELA cells were grown in high-glucose DMEM media supplemented with FBS10%, Sodium Pyruvate 1mM and gentamicin (20 mg/ml; all obtained from GIBCO) Flp-In T-REx 293 cells (Invitrogen), were grown in high-glucose DMEM (Wisent) supplemented with 10% fetal bovine serum, 500 units/ml penicillin, and 500 μg/ml streptomycin. All cell lines were kept in 5% CO_2 incubator at 37° C.

METHOD DETAILS

Ambulatory nocturnal activity behavioral test—Spontaneous ambulatory movement of mice was recorded using the Opto-M3 activity meter (Columbus Instruments) equipped

with infrared beams along the cage. Movement was counted as the number of times the infrared beams were disrupted. Mice were housed individually in a new cage 30 minutes prior to their daily dark cycle and ambulatory counts were recorded for a period of 12 hours (6:30 pm to 6:30 am).

Rotarod behavior test—Mouse motor coordination was tested at different ages using a Rotarod (IITC 755 Life Sciences) set at a ramp speed of 6 to 20 rpm over 180 s. The test consisted of three trials performed for each animal at the corresponding age and the latency to fall was recorded. Mice that completed the task received a final latency time of 180 s. Animals were trained in the rotarod two times of three trials each about 2 weeks prior to the first test.

Open field behavior test—Open field (Med Associates Inc.) is a sensitive method for measuring gross and fine locomotor activity. It consists of a chamber and a system of 16 infrared transmitters that record the position of the animal in the three-dimensional space. With this system not only, the horizontal movement can be recorded, but also the rearing activity. For our study, the animals were placed in the chamber 30 minutes before the test and the locomotor activities were recorded for 30 minutes.

Histology—Anesthetized mice were transcardially perfused with ice-cold PBS and 4% PFA. The brains were isolated, and regions of interest were dissected using a brain matrix, cryoprotected in sucrose 30%, and frozen in OCT. Frontal and sagittal sections were cut at a 20 μm thickness with a cryostat (Leica). Hematoxylin and Eosin (H&E) staining was done following standard procedures to study the anatomy of the brains.

Transmission electron microscopy—Hippocampus region from *Atad3* nKO mice and controls at 2 and 5 months (Bregma 3.28) were fixed in 2% glutaraldehyde in 0.05M phosphate buffer and 100mM sucrose, post-fixed overnight in 1% osmium tetroxide in 0.1M phosphate buffer, dehydrated through a series of graded ethanols, and embedded in a mixture of EM-bed/Araldite (Electron Microscopy Sciences). 1 μm thick sections were stained with Richardson's stain for observation under a light microscope. CA1 region was selected for ultra-thin 100nM sections which were cut on a Leica Ultracut-R ultramicrotome and stained with uranyl acetate and lead citrate. The grids were viewed at 80 kV in a JEOL JEM-1400 transmission electron microscope and images captured by an AMT BioSprint digital camera."

The "polygon selection" to define ROIs from the Fiji (Just ImageJ) software (National Institutes of Health) was used to trace and quantify mitochondrial morphometric parameters after setting the pixel size value according to the scale bar of the tiff images. For quantification of mitochondrial size, we averaged the mitochondrial area and perimeter values. For quantification of cristae area and perimeter, we averaged the total cristae areas and perimeters per mitochondrion, and then the ratios of control and *Atad3* nKO mitochondria. Measurements for each ROI were exported to Excel and analyzed using GraphPad prism 7. Data represents mean values per mitochondrion on 3 different images of each, Atad3 control and nKO mouse CA1 regions.

Quantitative PCR of genomic DNA—Genomic DNA was extracted from cortex and hippocampus using standard proteinase K, phenol, chloroform extraction and isopropyl alcohol precipitation. The ratio of mtDNA to nDNA was determined by quantitative real-time PCR using 10 ng of genomic DNA in a 20 μL reaction mixture using SsoFast EvaGreen Supermix (Bio-Rad) following PCR conditions stipulated by the manufacturer in a CFX96 Real Time PCR system (Bio-Rad). Primers for mtDNA were ND1-F: 5′-CAGCCTGACCCATAGCCATA-3′ and ND1-B: 5′-ATTCTCCTTCTGTCAGGTCGAA-3′ and for genomic DNA β-actin-F: 5′-GCGCAAGTACTCTGTGTGGA-3′ and β-actin-B: 5′-CATCGTACTCCTGCTTGCTG-3′. DNA amounts were quantified using the Ct method and expressed as a ratio of ND1/actin.

Western blots—Protein extracts were prepared from the cortex and hippocampus regions and homogenized in PBS containing a protease inhibitor mixture (Roche). Upon use, SDS was added to the homogenate at the final concentration of 4%. Homogenates were then centrifuged at 14,000g at 4°C, and the supernatant was collected for analysis. Protein concentration was determined by the Lowry assay using the BCA kit (Bio-Rad). Approximately 20–40 μg protein was separated by SDS-PAGE in 4%–20% acrylamide gels and transferred to PVDF membranes (Bio-Rad). Membranes were blocked with 5% nonfat milk in 0.1% Tween-20 in PBS and subsequently incubated with specific antibodies, which were incubated overnight at 4°C. Antibodies against NDUFB8, SDHA, UQCRC2, COXI, ATPase-a, vinculin and VDAC1 were obtained from Abcam (1:1000); β-actin and tubulin were obtained from Millipore Sigma (1:5000); Rabbit anti-ATAD3 was obtained from GenScript pre-immune Serum 1 (SC1088) (1:500); TUJ1 was obtained from Covance (1:10,0000); and Anti GAPDH from Ambion (1:10,000). Secondary antibodies conjugated to horseradish peroxidase (Cell Signaling Technology) were used, and the reaction was developed by chemiluminescence using SuperSignal West reagent (Thermo Fisher Scientific). Blots were visualized with Chemidoc Imaging System (Bio-Rad). Optical density measurements were taken by software supplied by Bio-Rad.

Mitochondria enriched isolated from cortex tissue was obtained by differential centrifugation as described before (Fernández-Vizarra et al., 2010). Briefly, cortex tissue was homogenized in mitochondria medium buffer with 15-20 strokes using a Dounce-type glass (with a manual driven glass pestle) and spun at low speed (1000 g for 5 min at 4C). The resulting supernatant was centrifugated at high speed (9,000 g during 2 min at 4C) and the mitochondria pellet was washed twice. Final mitochondria crude pellet was resuspended in mitochondria medium buffer before quantification. 10 μg of protein was separated by PAGE, transferred to a PVDF membrane (Bio-Rad), and incubated sequentially with ATAD3 (Proteintech, 1:1000); and VDAC1 antibodies (Abcam, 1:2000).

Blue Native PAGE—To identify and estimate the levels of respiratory supercomplexes, homogenates from hippocampus were treated with digitonin (ratio 1:8, protein/digitonin; Roche), and mitochondrial complexes were separated by BN–PAGE in 3%–12% acrylamide gradient gels (Invitrogen) (Diaz et al., 2009; Wittig et al., 2006). 10 μg of protein was separated by PAGE, transferred to a PVDF membrane (Bio-Rad), and incubated

sequentially with antibodies against several subunits of the different mitochondrial respiratory complexes.

Transcriptomics analysis—2.5-month-old *Atad3* nKO male mice and control littermates were transcardially perfused with ice-cold PBS. Cortex tissues were dissected fast frozen and used for Total RNA extraction (5 biological replicates per group). Following RNA extraction using TRIZOL, samples were treated with Turbo ™ DNase (Invitrogen) and RNA concentration and Quality control RIN (RNA Integrity Number) values were measured using the 2100 Bioanalyzer. RNA-Seq libraries were prepared using Illumina TruSeq Stranded Total RNA Library Prep Gold with a modified RNA fragmentation time of 6 minutes, but otherwise according to manufacturer's instructions. RNA sample RIN ranged from 6.4–9.1. Input amounts were 250 ng based on sample concentration. All samples were subjected to 10 PCR amplification cycles. Libraries were balanced for pooling using fragment analysis (Agilent 5200) and DNA quantitation (Qubit). The library pool was sequenced on an Illumina NovaSeq 6000 on an S1 flow cell as 2x 100 bp reads. Base calling and demultiplexing was performed in BaseSpace® using default bcl2fastq parameters. RNA Sequencing data was analyzed using Illumina BaseSpace® application tools which included the Illumina TopHat Alignment, Cufflinks Assembly and Differential Expression analysis using DESeq2 normalization. GO term analysis enrichment was done using the DAVID functional annotation tool.

Metabolomic analysis—Cortex tissues from 2.5-month-old *Atad3* nKO male mice and control littermates were dissected, snap frozen, and analyzed by Metabolon's global Precision Metabolomics (https://www.metabolon.com/). Six biological replicates for controls and four for the *Atad3* nKO group were analyzed as described (Peralta et al., 2020). Bioinformatics analysis of data was done using metaboloanalyst (http://www.metaboanalyst.ca) and enrichment analysis was completed using gene list Enrichr (Kuleshov et al., 2016) enrichment analysis tool.

Lipidomic analysis—Cortex and hippocampus from 2.5-month-old *Atad3* nKO male mice and control littermates were dissected, deeply frozen, and analyzed by the Kansas Lipidomic Research Center (KLRC) at the Kansas State University, (https://www.k-state.edu/lipid/). Five biological replicates were processed from each group and prepared using a modified Bligh and Dyer procedure as described previously (Bligh and Dyer, 1959; Chan et al., 2012), spiked with appropriate internal standards, and analyzed using a 6490 Triple Quadrupole LC/MS system (Agilent Technologies). Glycerophospholipids and sphingolipids were separated with normal-phase HPLC as described previously (Chan et al., 2012), with a few modifications. An Agilent Zorbax Rx-Sil column (inner diameter 2.1×100 mm) was used under the following conditions: mobile phase A (chloroform:methanol:1 M ammonium hydroxide, 89.9:10:0.1, v/v) and mobile phase B (chloroform:methanol:water:ammonium hydroxide, 55:39.9:5:0.1, v/v); 95% A for 2 min, linear gradient to 30% A over 18 min and held for 3 min, and linear gradient to 95% A over 2 min and held for 6 min. Sterols and glycerolipids were separated with reverse-phase HPLC using an isocratic mobile phase as described previously (Chan et al., 2012), except with an Agilent Zorbax Eclipse XDB-C18 column (4.6×100 mm). Quantification of

lipid species was accomplished using multiple reaction monitoring (MRM) transitions that were developed in earlier studies (Chan et al., 2012) in conjunction with referencing of appropriate internal standards: PA 14:0/14:0, PC 14:0/14:0, PE 14:0/14:0, PI 12:0/13:0, PS 14:0/14:0, SM d18:1/12:0, D7-cholesterol, CE 17:0, MG 17:0, 4ME 16:0 diether DG, D5-TG 16:0/18:0/16:0 (Avanti Polar Lipids).

Co-immunoprecipitation assay—Two mg of mitochondria isolated from HEK293T cells were extracted in 500 μL of extraction buffer (20 mM HEPES, pH 7.4, 150 mM KCl, 0.5 mM PMSF, EDTA-free protease inhibitor cocktail (Roche), 1% digitonin, and 10 mM $MgCl_2$). Mitochondrial proteins were incubated with α-IgG (control), or α-ATAD3 conjugated Dynabeads (Life Technologies) at room temperature for 4 h. Following several antibody tests, the rabbit polyclonal anti-ATAD3 antibody-N-terminal from Abcam yielded efficient immunoprecipitation results. The supernatant containing unbound material was subsequently removed and the beads were washed 5 times with low-salt NET-2 buffer (50mM Tris-HCl pH 7.4, 150 mM NaCl, 0.05% NP-40, EDTA-free protease inhibitor cocktail (Roche)), or high-salt NET-2 buffer (with 300 mM NaCl), and once with 1X PBS. The bound proteins were eluted using dye-less buffer, precipitated with methanol/chloroform, and analyzed by mass spectrometry at the Keck Biotechnology Resource Laboratory (Yale University School of Medicine, New Haven, CT) as described (Tu and Barrientos, 2015). To analyze the interactome, hits with higher difference between IgG control and found ATAD3A were used for further analysis. Go terms were identified with enrichment analysis using gene list Enrichr analysis tool.

BioID proximity labeling

Cloning of Atad3a: *Mus musculus* ATPase family, AAA domain containing 3A (Atad3a), mRNA (NM_179203.3) was synthesized as a gBlock gene fragment (IDT, the custom biology company) and subcloned in the pcDNA5-pDEST-BirA-Flag C-terminal vector using the In-fusion HD cloning procedure (Clontech Laboratories, Inc). For this, the vector plasmid was initially linearized after digestion with BSRG1 HF followed by infusion reaction performed at 2:1 ratio (insert/vector). Final plasmid was transformed into stellar competent cells, grown overnight at 37C in LB media supplemented with Ampicillin 100 μg/ml and final construct DNA confirmed by sequencing.

Site directed mutagenesis—The substitution of glycine 355 to aspartate (G355D) present in humans was made in the conserved region of the mouse ATAD3 protein (NP_849534). Using the QuikChange XL site-Directed Mutagenesis kit (Agilent technologies). Two nucleotides at position 1059- GGA encoding for Glutamine were changed to 1059- GAC encoding for Aspartate using the overlapping primers (forward 5′-cgggccacctgacacagggaagac-3′) and (Reverse 5′-gtcttccctgtgtcaggtggcccg-3′). Final mutated ATAD3A was confirmed by sequencing.

Generation of isogenic cell lines with the ATAD3 wild-type and mutated protein baits, purification, and identification by mass spectrometry of biotinylated proteins, was performed as described previously (Antonicka et al., 2020). All preys detected with False Discovery Rare (BFDR) cutoff of   0.01 are listed and fold change used to determine the top prey

hits. Comparison among interactors was analyzed using the plug-in Jvenn diagrams (Bardou et al., 2014) to identify common and unique interactor among groups. Gene set enrichment analysis was used to identify the GO terms using Enrichr web server.

NanoBit protein complementation assay

Cloning: Human LETM1 (g blocks V.3 CDNA) (NM_015416.5) was cloned into the (Small Bit) SmBiT flexi vector at N or C-terminal ends (pFN35K SmBiT TK-neoFlexi® Vector and pFC36K SmBiT TK-neoFlexi® Vector) using infusion reactions (TAKARA). Human ATAD3A (g blocks V.3 CDNA) (NM_018188.5) was cloned into the (Large Bit) pFC34K LgBiT TK-neoFlexi® Vector. SmBiT-PRKACA Control Vector and LgBiT-PRKAR2A Control Vector were used as a positive control and a re-circularized version of the empty LgBiT (pFN33K LgBiT TK-neoFlexi® Vector) and NanoBiT® Halo tag protein Control were used as negative control vectors. Confirmation of proper Localizations was done by immunofluorescence using Anti-NanoLuc® Monoclonal Antibody (Promega 1:500) and TIM23 (BD Bioscience, 1:1000).

Assay—Approximately 1.25×10^5 HEK293T cells were seeded in 24 cell wells in DMEM media supplemented with FBS10%, Sodium Pyruvate 1mM. Cells were co-transfected using GeneJet at a ratio 3:1 (Lipid to DNA) with a total concentration of 500 ng per well (250ng per each plasmid). Cells were incubated at 37C in a 5% Co2 incubator for 20 hours and localization by immunofluorescence was tested using the antibodies from mitochondria and LgBiT. After that, cells were trypsinized and re-plated into a pre-coated (poly-L-lysine) white opaque 96 well tissue culture plates. Five technical replicates were used per plasmid combination. Followed by incubation for 4 more hours for cell attachment. Assay was performed according to the manufacture instructions. Luminescence was monitored at 37C for 30 minutes. The average of maximum luminescence points (10 min to 30 min) RLU was used for calculations.

Super-resolution microscopy

Immunostaining: Approximately 1×10^4 HELA cells (Passage P3 to P5) were grown in high-glucose DMEM supplemented with fetal bovine serum (10%; Sigma), sodium pyruvate (1 mM), and gentamicin (20 mg/ml; all obtained from GIBCO). Cells were plated in μ-slide 4 well glass bottom chambers the day before the staining. Initially, cells were washed once with PBS and fixed with 3% paraformaldehyde (PFA) /0.1% glutaraldehyde for 10 min followed by a reduction with 0.1% NaBH4 for 7 minutes at room temperature. Then, cells were washed 3 times (each for 5 minutes) with PBS. Permeabilization was done with Triton/PBS 0.5% for 15 minutes and blocked for 90 minutes with 10% NGS/ 0.1% Triton/PBS at room temperature. Primary antibodies were diluted in 5% NGS/0.1% Triton/PBS and incubated for 60 minutes, followed by 5 washes (15 minutes per wash) with 1%NGS/0.1% Triton/PBS at room temperature. Secondary antibodies were diluted in 5% NGS/0.1% Triton/PBS and incubated for 30 minutes followed by 5 washes (15 minutes per wash) with 1%NGS/0.1% Triton//PBS at room temperature. The final washes included first PBS 3 times (5 minutes per wash) followed by 2 washes (3 minutes each) with dH_2O.

Primary Antibody	Catalog	Company	Clonality	Dilution
ATAD3 N-terminal	16610-1-AP	Proteintech	Rabbit polyclonal	1:100
ATAD3 C-terminal	sc-376185	Santacruz	Mouse monoclonal	1:50
ATAD3B(A-8)	sc-514615	Santacruz	Mouse monoclonal	1:50
TOM20 (F-10)	sc-17764	Santacruz	Mouse monoclonal	1:100
TOM20	HPA011562	Sigma-Aldrich	Rabbit polyclonal	1:100
TIM23	611222	BD Biosciences	Mouse monoclonal	1:100
ANTI-DNA	CBL186-EMD	MILLIPORE	Mouse monoclonal	1:100
Secondary Antibody				
Anti-rabbit	NBP1-72732JF646	Novus biologicals	Rabbit polyclonal	1:500
Anti-mouse	A-11004	Thermo-Fisher	Mouse polyclonal	1:500

STORM imaging and processing—TIRF Imaging experiments were done with a Nikon eclipse Ti2 inverted microscope equipped with Nikon Instruments (N-STORM). A 100x TIRF objective 1.49NA objective lens was utilized and imaged using a Hamamatsu C11440 ORCA-flash CMOS 4.0 camera. Images were acquired sequentially 10,000 frames per filter channel at 20ms time duration. Cells labeled with JF646 secondary labeled were excited with 90% laser power from a 647 nm laser and A568 secondary labeled cells were excited with a 561nm laser at 100% laser power. Nikon Nd2 files were separated and converted to tiff files per channel by custom python script. STORM localization analysis was carried out with either ImageJ, thunderstorm plugin (1.3-2014-11-08) or WindSTORM MATLAB code. Data was fitted with Gaussian PSF model using weighted least-squares estimation for thunderstorm plugin.

Colocalization analysis—Localization data files were then used in colocalization analysis using Coloc-Tesseler software. Data localization file associated with the secondary protein antibody using the JF646 is imported as dataset1 and data localization file associated with the secondary protein using the A568 is imported as dataset2. Either a region of interest was manually selected or the whole image was used to calculate the colocalization coefficients. Mander's statistical test is calculated for dataset1 protein localization with dataset2 protein localization as well as dataset2 protein localization with dataset1. Values are then exported and analyzed using GraphPad Prism 7.

Cluster analysis—Quantification of the ATAD3 clusters was done using the SR-Tesseler version 1.0.0.1 and the Single molecule localization obtained from each antibody staining (Antibody against the ATAD3 N-terminal, ATAD3 C-terminal and ATAD3B). Localization analysis output from WindSTORM was imported into the software. Voronoi diagram was computed over the number of localizations detected after blinking correction (default fixed pixel size of 0.3). Object segmentation was performed on the complete Voronoi diagram using a shortest distance parameter $1i < 50$ nm and 50 as the minimum number of localizations per object. Cluster detection was computed on each object using a density parameter threshold of double the individual particle average density ($\delta 1i > 2\delta$) with a

minimum 50 detections per cluster. GraphPad Prism 7 was used to represent the frequency distribution histograms of the calculated diameter for each cluster (in nm). Data was fit to a Gaussian function to obtain best fit values for the fitted curve.

Periodicity analysis

Tracing and intensity profile calculations: Reconstructed single plane STORM images were imported into ImageJ and used for tracing antibody signal from different HeLa cells. Split Tiff files were converted into 8-bit images for tracing purposes. The ImageJ script were used to generate stacks folders for the channel of interest as described (Vassilopoulos et al., 2019). Intensity profile measurements were calculated following the "Measure ROI" macro set tools. A total of 560 tracings from the ATAD3 N-terminal raw signal were generated from 9 different HeLa cells. Intensity profiles were calculated for each cell and data exported for periodicity analysis.

Periodicity was calculated using Fourier transform function (FFT) in MATLAB utilizing the values from Intensity profiles generated previously. For each Fourier-transformed trace, peaks that exceeded an amplitude threshold of 50% of the maximum peak amplitude were selected for periodicity calculation. Frequency distribution of the total number of calculated periods (in nm) was analyzed using GraphPad prism 7. Histogram of the frequency data was fit to a Gaussian function to obtain best fit values for the fitted curve.

Data mining—CF-MS was analyzed at https://fosterlab.github.io/CF-MS-analysis. Analysis of Tafazzin mutant samples was done using Supplementary figure S3 of reference (Van Strien et al., 2019). Analysis of neonate brain samples was done using Supplementary table S1 of reference (Stepanova et al., 2019). Heatmaps were generated in Excel.

QUANTIFICATION AND STATISTICAL ANALYSIS

Bars represent means ± standard error (SEM) or standard deviation (SD) as specified. P values were calculated by *Student's t test, ANOVA* as applicable to determine the level of statistical difference and GraphPad Prism 7 software for presentation. -n.s. indicates not statistically significant; $* p < 0.05$, $**p < 0.01$ and $***p < 0.0001$ indicates significance.

Supplementary Material

Refer to Web version on PubMed Central for supplementary material.

ACKNOWLEDGMENTS

REFERENCES

Antonicka H, Lin ZY, Janer A, Aaltonen MJ, Weraarpachai W, Gingras AC, and Shoubridge EA (2020). A High-Density Human Mitochondrial Proximity Interaction Network. Cell Metab. 32, 479–497.e9. [PubMed: 32877691]

Austin S, and Nowikovsky K (2019). LETM1: Essential for Mitochondrial Biology and Cation Homeostasis? Trends Biochem. Sci 44, 648–658. [PubMed: 31101453]

Bardou P, Mariette J, Escudié F, Djemiel C, and Klopp C (2014). jvenn: an interactive Venn diagram viewer. BMC Bioinformatics 15, 293. [PubMed: 25176396]

Baudier J (2018). ATAD3 proteins: brokers of a mitochondria-endoplasmic reticulum connection in mammalian cells. Biol. Rev. Camb. Philos. Soc 93, 827–844. [PubMed: 28941010]

Bauerschmitt H, Mick DU, Deckers M, Vollmer C, Funes S, Kehrein K, Ott M, Rehling P, and Herrmann JM (2010). Ribosome-binding proteins Mdm38 and Mba1 display overlapping functions for regulation of mitochondrial translation. Mol. Biol. Cell 21, 1937–1944. [PubMed: 20427570]

Bligh EG, and Dyer WJ (1959). A rapid method of total lipid extraction and purification. Can. J. Biochem. Physiol 37, 911–917. [PubMed: 13671378]

Chan RB, Oliveira TG, Cortes EP, Honig LS, Duff KE, Small SA, Wenk MR, Shui G, and Di Paolo G (2012). Comparative lipidomic analysis of mouse and human brain with Alzheimer disease. J. Biol. Chem 287, 2678–2688. [PubMed: 22134919]

Chicco AJ, and Sparagna GC (2007). Role of cardiolipin alterations in mitochondrial dysfunction and disease. Am. J. Physiol. Cell Physiol 292, C33–C44. [PubMed: 16899548]

Cooper HM, Yang Y, Ylikallio E, Khairullin R, Woldegebriel R, Lin KL, Euro L, Palin E, Wolf A, Trokovic R, et al. (2017). ATPase-deficient mitochondrial inner membrane protein ATAD3A disturbs mitochondrial dynamics in dominant hereditary spastic paraplegia. Hum. Mol. Genet 26, 1432–1443. [PubMed: 28158749]

de la Peña AH, Goodall EA, Gates SN, Lander GC, and Martin A (2018). Substrate-engaged 26S proteasome structures reveal mechanisms for ATP-hydrolysis-driven translocation. Science 362. 10.1126/science.aav0725.

Desai R, Frazier AE, Durigon R, Patel H, Jones AW, Dalla Rosa I, Lake NJ, Compton AG, Mountford HS, Tucker EJ, et al. (2017). ATAD3 gene cluster deletions cause cerebellar dysfunction associated with altered mitochondrial DNA and cholesterol metabolism. Brain 140, 1595–1610. [PubMed: 28549128]

Diaz F, Barrientos A, and Fontanesi F (2009). Evaluation of the mitochondrial respiratory chain and oxidative phosphorylation system using blue native gel electrophoresis. Curr Protoc Hum Genet. Published online October 1, 2009. 10.1002/0471142905.hg1904s63.

Dorison N, Gaignard P, Bayot A, Gelot A, Becker PH, Fourati S, Lebigot E, Charles P, Wai T, Therond P, and Slama A (2020). Mitochondrial dysfunction caused by novel ATAD3A mutations. Mol. Genet. Metab 131, 107–113. [PubMed: 32933822]

Dragatsis I, and Zeitlin S (2000). CaMKIIalpha-Cre transgene expression and recombination patterns in the mouse brain. Genesis 26, 133–135. [PubMed: 10686608]

Fajardo VA, Mikhaeil JS, Leveille CF, Saint C, and LeBlanc PJ (2017). Cardiolipin content, linoleic acid composition, and tafazzin expression in response to skeletal muscle overload and unload stimuli. Sci. Rep 7, 2060. [PubMed: 28515468]

Fang HY, Chang CL, Hsu SH, Huang CY, Chiang SF, Chiou SH, Huang CH, Hsiao YT, Lin TY, Chiang IP, et al. (2010). ATPase family AAA domain-containing 3A is a novel anti-apoptotic factor in lung adenocarcinoma cells. J. Cell Sci 123, 1171–1180. [PubMed: 20332122]

Fernández-Vizarra E, Ferrín G, Pérez-Martos A, Fernández-Silva P, Zeviani M, and Enríquez JA (2010). Isolation of mitochondria for biogenetical studies: An update. Mitochondrion 10, 253–262. [PubMed: 20034597]

Frazier AE, Compton AG, Kishita Y, Hock DH, Welch AE, Amarasekera SSC, Rius R, Formosa LE, Imai-Okazaki A, Francis D, et al. (2021). Fatal perinatal mitochondrial cardiac failure caused by recurrent de novo duplications in the ATAD3 locus. Med (N Y) 2, 49–73. [PubMed: 33575671]

Gates SN, and Martin A (2020). Stairway to translocation: AAA+ motor structures reveal the mechanisms of ATP-dependent substrate translocation. Protein Sci. 29, 407–419. [PubMed: 31599052]

Gates SN, Yokom AL, Lin J, Jackrel ME, Rizo AN, Kendsersky NM, Buell CE, Sweeny EA, Mack KL, Chuang E, et al. (2017). Ratchet-like polypeptide translocation mechanism of the AAA+ disaggregase Hsp104. Science 357, 273–279. [PubMed: 28619716]

Gerhold JM, Cansiz-Arda , Lõhmus M, Engberg O, Reyes A, van Rennes H, Sanz A, Holt IJ, Cooper HM, and Spelbrink JN (2015). Human Mitochondrial DNA-Protein Complexes Attach to a Cholesterol-Rich Membrane Structure. Sci. Rep 5, 15292. [PubMed: 26478270]

Gilquin B, Taillebourg E, Cherradi N, Hubstenberger A, Gay O, Merle N, Assard N, Fauvarque MO, Tomohiro S, Kuge O, and Baudier J (2010). The AAA+ ATPase ATAD3A controls mitochondrial dynamics at the interface of the inner and outer membranes. Mol. Cell. Biol 30, 1984–1996. [PubMed: 20154147]

Goller T, Seibold UK, Kremmer E, Voos W, and Kolanus W (2013). Atad3 function is essential for early post-implantation development in the mouse. PLoS ONE 8, e54799. [PubMed: 23372768]

Gunning AC, Strucinska K, Muñoz Oreja M, Parrish A, Caswell R, Stals KL, Durigon R, Durlacher-Betzer K, Cunningham MH, Grochowski CM, et al. (2020). Recurrent De Novo NAHR Reciprocal Duplications in the ATAD3 Gene Cluster Cause a Neurogenetic Trait with Perturbed Cholesterol and Mitochondrial Metabolism. Am. J. Hum. Genet 106, 272–279. [PubMed: 32004445]

Hanson PI, and Whiteheart SW (2005). AAA+ proteins: have engine, will work. Nat. Rev. Mol. Cell Biol 6, 519–529. [PubMed: 16072036]

Harel T, Yoon WH, Garone C, Gu S, Coban-Akdemir Z, Eldomery MK, Posey JE, Jhangiani SN, Rosenfeld JA, Cho MT, et al. ; Baylor-Hopkins Center for Mendelian Genomics; University of Washington Center for Mendelian Genomics (2016). Recurrent De Novo and Biallelic Variation of ATAD3A, Encoding a Mitochondrial Membrane Protein, Results in Distinct Neurological Syndromes. Am. J. Hum. Genet 99, 831–845. [PubMed: 27640307]

He J, Cooper HM, Reyes A, Di Re M, Sembongi H, Litwin TR, Gao J, Neuman KC, Fearnley IM, Spinazzola A, et al. (2012). Mitochondrial nucleoid interacting proteins support mitochondrial protein synthesis. Nucleic Acids Res. 40, 6109–6121. [PubMed: 22453275]

Hoffmann M, Bellance N, Rossignol R, Koopman WJ, Willems PH, Mayatepek E, Bossinger O, and Distelmaier F (2009). C. elegans ATAD-3 is essential for mitochondrial activity and development. PLoS ONE 4, e7644. [PubMed: 19888333]

Houten SM, Violante S, Ventura FV, and Wanders RJ (2016). The Biochemistry and Physiology of Mitochondrial Fatty Acid β-Oxidation and Its Genetic Disorders. Annu. Rev. Physiol 78, 23–44. [PubMed: 26474213]

Hubstenberger A, Merle N, Charton R, Brandolin G, and Rousseau D (2010). Topological analysis of ATAD3A insertion in purified human mitochondria. J. Bioenerg. Biomembr 42, 143–150. [PubMed: 20349121]

Issop L, Fan J, Lee S, Rone MB, Basu K, Mui J, and Papadopoulos V (2015). Mitochondria-associated membrane formation in hormone-stimulated Leydig cell steroidogenesis: role of ATAD3. Endocrinology 156, 334–345. [PubMed: 25375035]

Jin G, Xu C, Zhang X, Long J, Rezaeian AH, Liu C, Furth ME, Kridel S, Pasche B, Bian XW, and Lin HK (2018). Atad3a suppresses Pink1-dependent mitophagy to maintain homeostasis of hematopoietic progenitor cells. Nat. Immunol 19, 29–40. [PubMed: 29242539]

Johnson SC, Yanos ME, Kayser EB, Quintana A, Sangesland M, Castanza A, Uhde L, Hui J, Wall VZ, Gagnidze A, et al. (2013). mTOR inhibition alleviates mitochondrial disease in a mouse model of Leigh syndrome. Science 342, 1524–1528. [PubMed: 24231806]

Kühlbrandt W (2019). Structure and Mechanisms of F-Type ATP Synthases. Annu. Rev. Biochem 88, 515–549. [PubMed: 30901262]

Kuleshov MV, Jones MR, Rouillard AD, Fernandez NF, Duan Q, Wang Z, Koplev S, Jenkins SL, Jagodnik KM, Lachmann A, et al. (2016). Enrichr: a comprehensive gene set enrichment analysis web server 2016 update. Nucleic Acids Res. 44 (W1), W90–W97. [PubMed: 27141961]

Lang L, Loveless R, and Teng Y (2020). Emerging Links between Control of Mitochondrial Protein ATAD3A and Cancer. Int. J. Mol. Sci 21. 10.3390/ijms21217917.

Levet F, Hosy E, Kechkar A, Butler C, Beghin A, Choquet D, and Sibarita JB (2015). SR-Tesseler: a method to segment and quantify localization-based super-resolution microscopy data. Nat Methods. 12, 1065–1071. [PubMed: 26344046]

Levet F, Julien G, Galland R, Butler C, Beghin A, Chazeau A, Hoess P, Ries J, Giannone G, and Sibarita JB (2019). A tessellation-based colocalization analysis approach for single-molecule localization microscopy. Nat Commun. 10, 2379. [PubMed: 31147535]

Lin QT, and Stathopulos PB (2019). Molecular Mechanisms of Leucine Zipper EF-Hand Containing Transmembrane Protein-1 Function in Health and Disease. Int. J. Mol. Sci 20. 10.3390/ijms20020286.

Maltecca F, Baseggio E, Consolato F, Mazza D, Podini P, Young SM Jr., Drago I, Bahr BA, Puliti A, Codazzi F, et al. (2015). Purkinje neuron Ca2+ influx reduction rescues ataxia in SCA28 model. J. Clin. Invest 125, 263–274. [PubMed: 25485680]

Mejia EM, and Hatch GM (2016). Mitochondrial phospholipids: role in mitochondrial function. J. Bioenerg. Biomembr 48, 99–112. [PubMed: 25627476]

Merle N, Féraud O, Gilquin B, Hubstenberger A, Kieffer-Jacquinot S, Assard N, Bennaceur-Griscelli A, Honnorat J, and Baudier J (2012). ATAD3B is a human embryonic stem cell specific mitochondrial protein, re-expressed in cancer cells, that functions as dominant negative for the ubiquitous ATAD3A. Mitochondrion 12, 441–448. [PubMed: 22664726]

Miller JM, and Enemark EJ (2016). Fundamental Characteristics of AAA+ Protein Family Structure and Function. Archaea 2016, 9294307. [PubMed: 27703410]

Mizuarai S, Miki S, Araki H, Takahashi K, and Kotani H (2005). Identification of dicarboxylate carrier Slc25a10 as malate transporter in de novo fatty acid synthesis. J. Biol. Chem 280, 32434–32441. [PubMed: 16027120]

Nakamura S, Matsui A, Akabane S, Tamura Y, Hatano A, Miyano Y, Omote H, Kajikawa M, Maenaka K, Moriyama Y, et al. (2020). The mitochondrial inner membrane protein LETM1 modulates cristae organization through its LETM domain. Commun. Biol 3, 99. [PubMed: 32139798]

Nelo-Bazán MA, Latorre P, Bolado-Carrancio A, Pérez-Campo FM, Echenique-Robba P, Rodríguez-Rey JC, and Carrodeguas JA (2016). Early growth response 1 (EGR-1) is a transcriptional regulator of mitochondrial carrier homolog 1 (MTCH 1)/presenilin 1-associated protein (PSAP). Gene 578, 52–62. [PubMed: 26692143]

Osman C, Merkwirth C, and Langer T (2009). Prohibitins and the functional compartmentalization of mitochondrial membranes. J. Cell Sci 122, 3823–3830. [PubMed: 19889967]

Ovesný M, K ížek P, Borkovec J, Svindrych Z, and Hagen GM (2014). ThunderSTORM: a comprehensive ImageJ plug-in for PALM and STORM data analysis and super-resolution imaging. Bioinformatics. 30, 2389–2390. [PubMed: 24771516]

Peralta S, Goffart S, Williams SL, Diaz F, Garcia S, Nissanka N, Area-Gomez E, Pohjoismäki J, and Moraes CT (2018). ATAD3 controls mitochondrial cristae structure in mouse muscle, influencing mtDNA replication and cholesterol levels. J. Cell Sci 131. 10.1242/jcs.217075.

Peralta S, González-Quintana A, Ybarra M, Delmiro A, Pérez-Pérez R, Docampo J, Arenas J, Blázquez A, Ugalde C, and Martín MA (2019). Novel ATAD3A recessive mutation associated to fatal cerebellar hypoplasia with multiorgan involvement and mitochondrial structural abnormalities. Mol. Genet. Metab 128, 452–462. [PubMed: 31727539]

Peralta S, Pinto M, Arguello T, Garcia S, Diaz F, and Moraes CT (2020). Metformin delays neurological symptom onset in a mouse model of neuronal complex I deficiency. JCI Insight 5. 10.1172/jci.insight.141183.

Poston CN, Krishnan SC, and Bazemore-Walker CR (2013). In-depth proteomic analysis of mammalian mitochondria-associated membranes (MAM). J. Proteomics 79, 219–230. [PubMed: 23313214]

Puchades C, Ding B, Song A, Wiseman RL, Lander GC, and Glynn SE (2019). Unique Structural Features of the Mitochondrial AAA+ Protease AFG3L2 Reveal the Molecular Basis for Activity in Health and Disease. Mol. Cell 75, 1073–1085.e6. [PubMed: 31327635]

Rust MJ, Bates M, and Zhuang X (2006). Sub-diffraction-limit imaging by stochastic optical reconstruction microscopy (STORM). Nat. Methods 3, 793–795. [PubMed: 16896339]

Salewskij K, Rieger B, Hager F, Arroum T, Duwe P, Villalta J, Colgiati S, Richter CP, Psathaki OE, Enriquez JA, et al. (2020). The spatio-temporal organization of mitochondrial F_1F_O ATP synthase in cristae depends on its activity mode. Biochim. Biophys. Acta Bioenerg 1861, 148091. [PubMed: 31669489]

Scorrano L, De Matteis MA, Emr S, Giordano F, Hajnóczky G, Kornmann B, Lackner LL, Levine TP, Pellegrini L, Reinisch K, et al. (2019). Coming together to define membrane contact sites. Nat. Commun 10, 1287. [PubMed: 30894536]

Signorile A, Sgaramella G, Bellomo F, and De Rasmo D (2019). Prohibitins: A Critical Role in Mitochondrial Functions and Implication in Diseases. Cells 8. 10.3390/cells8010071.

Skinnider MA, and Foster LJ (2021). Meta-analysis defines principles for the design and analysis of co-fractionation mass spectrometry experiments. Nat. Methods 18, 806–815. [PubMed: 34211188]

Stepanova A, Sosunov S, Niatsetskaya Z, Konrad C, Starkov AA, Manfredi G, Wittig I, Ten V, and Galkin A (2019). Redox-Dependent Loss of Flavin by Mitochondrial Complex I in Brain Ischemia/Reperfusion Injury. Antioxid. Redox Signal. 31, 608–622.

Surovtseva YV, Shutt TE, Cotney J, Cimen H, Chen SY, Koc EC, and Shadel GS (2011). Mitochondrial ribosomal protein L12 selectively associates with human mitochondrial RNA polymerase to activate transcription. Proc. Natl. Acad. Sci. USA 108, 17921–17926. [PubMed: 22003127]

Tamai S, Iida H, Yokota S, Sayano T, Kiguchiya S, Ishihara N, Hayashi J, Mihara K, and Oka T (2008). Characterization of the mitochondrial protein LETM1, which maintains the mitochondrial tubular shapes and interacts with the AAA-ATPase BCS1L. J. Cell Sci 121, 2588–2600. [PubMed: 18628306]

Thomas PS Jr., Fraley GS, Damian V, Woodke LB, Zapata F, Sopher BL, Plymate SR, and La Spada AR (2006). Loss of endogenous androgen receptor protein accelerates motor neuron degeneration and accentuates androgen insensitivity in a mouse model of X-linked spinal and bulbar muscular atrophy. Hum. Mol. Genet 15, 2225–2238. [PubMed: 16772330]

Tu YT, and Barrientos A (2015). The Human Mitochondrial DEAD-Box Protein DDX28 Resides in RNA Granules and Functions in Mitoribosome Assembly. Cell Rep. 10, 854–864. [PubMed: 25683708]

van den Ecker D, Hoffmann M, Müting G, Maglioni S, Herebian D, Mayatepek E, Ventura N, and Distelmaier F (2015). Caenorhabditis elegans ATAD-3 modulates mitochondrial iron and heme homeostasis. Biochem. Biophys. Res. Commun 467, 389–394. [PubMed: 26427876]

Van Strien J, Guerrero-Castillo S, Chatzispyrou IA, Houtkooper RH, Brandt U, and Huynen MA (2019). COmplexome Profiling ALignment (COPAL) reveals remodeling of mitochondrial protein complexes in Barth syndrome. Bioinformatics 35, 3083–3091. [PubMed: 30649188]

Vance JE (2020). Inter-organelle membrane contact sites: implications for lipid metabolism. Biol. Direct 15, 24. [PubMed: 33176847]

Vassilopoulos S, Gibaud S, Jimenez A, Caillol G, and Leterrier C (2019). Ultrastructure of the axonal periodic scaffold reveals a braid-like organization of actin rings. Nat. Commun 10, 5803. [PubMed: 31862971]

Wang L, and Walter P (2020). Msp1/ATAD1 in Protein Quality Control and Regulation of Synaptic Activities. Annu. Rev. Cell Dev. Biol 36, 141–164. [PubMed: 32886535]

Wittig I, Braun HP, and Schägger H (2006). Blue native PAGE. Nat. Protoc 1, 418–428. [PubMed: 17406264]

Wurm CA, Neumann D, Lauterbach MA, Harke B, Egner A, Hell SW, and Jakobs S (2011). Nanoscale distribution of mitochondrial import receptor Tom20 is adjusted to cellular conditions and exhibits an inner-cellular gradient. Proc. Natl. Acad. Sci. USA 108, 13546–13551. [PubMed: 21799113]

Xu Y, Malhotra A, Ren M, and Schlame M (2006). The enzymatic function of tafazzin. J. Biol. Chem 281, 39217–39224. [PubMed: 17082194]

Zhao Y, Sun X, Hu D, Prosdocimo DA, Hoppel C, Jain MK, Ramachandran R, and Qi X (2019). ATAD3A oligomerization causes neurodegeneration by coupling mitochondrial fragmentation and bioenergetics defects. Nat. Commun 10, 1371. [PubMed: 30914652]

Highlights

- Neurons show mitochondrial cristae abnormalities early when ATAD3 is knocked out

- Oxidative phosphorylation abnormalities are secondary

- ATAD3 interacts with several inner mitochondrial membrane proteins

- ATAD3 is regularly spaced within mitochondrial membranes
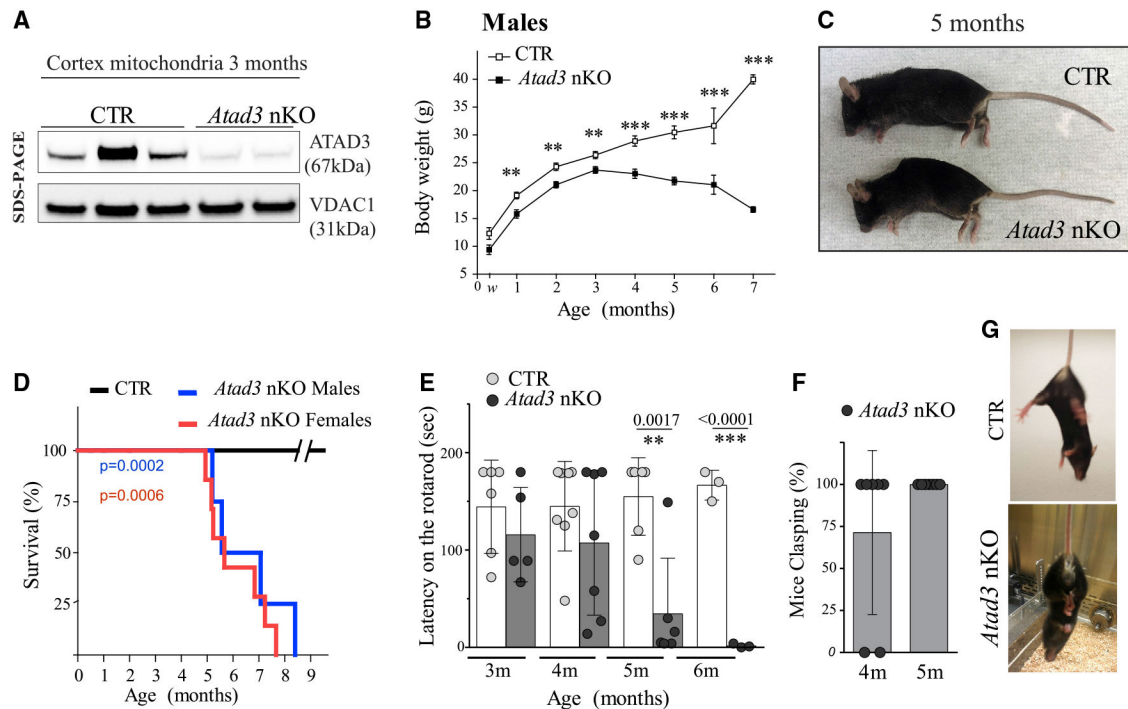
Figure 1. Characterization of *Atad3* nKO mice

(A) Western blot of ATAD3 protein in mitochondria from cortex of 3 months old control (CTR) and *Atad3* nKO mice, VDAC1 was probed to normalize the protein loading.

(B) Body weight comparison over time of *Atad3* nKO male mice (black squares; n = 6), age-matched control male mice (white squares; n = 7). *P*-values were calculated by *Student's t test*.

(C) Representative image of 5-month-old *Atad3* nKO mouse and a control (CTR) littermate.

(D) Survival curve of *Atad3* nKO female mice (red line) and male mice (blue line). *P*-values were calculated using the log-rank (Mantel-Cox) test. $p < 0.0002$ for female mice (n = 7 CTR *versus* n = 7 nKO); $p = 0.0006$ for male mice (n = 7 CTR *versus* n = 5 nKO). All *Atad3* nKO mice died before 8 months of age.

(E) Rotarod performed by *Atad3* nKO male mice and age-matched control mice at 3, 4, 5 and 6 months of age (n = 3–10). Data are represented as mean ± SD.

(F) Clasping of the limbs in *Atad3* nKO mice at 4 and 5 months of age. Bars represent means ± standard deviation (SD). *P*-values were calculated by *Student's t test* to determine the level of statistical difference; statistical significance is indicated by $*p < 0.05$, $**p < 0.01$ and $***p < 0.0001$.

(G) Representative image of a tail suspension test of 4-month-old Atad3 nKO and control littermates. Atad3 nKO mice have a typical paw-clasped posture, while control mice show a normal flexion response.
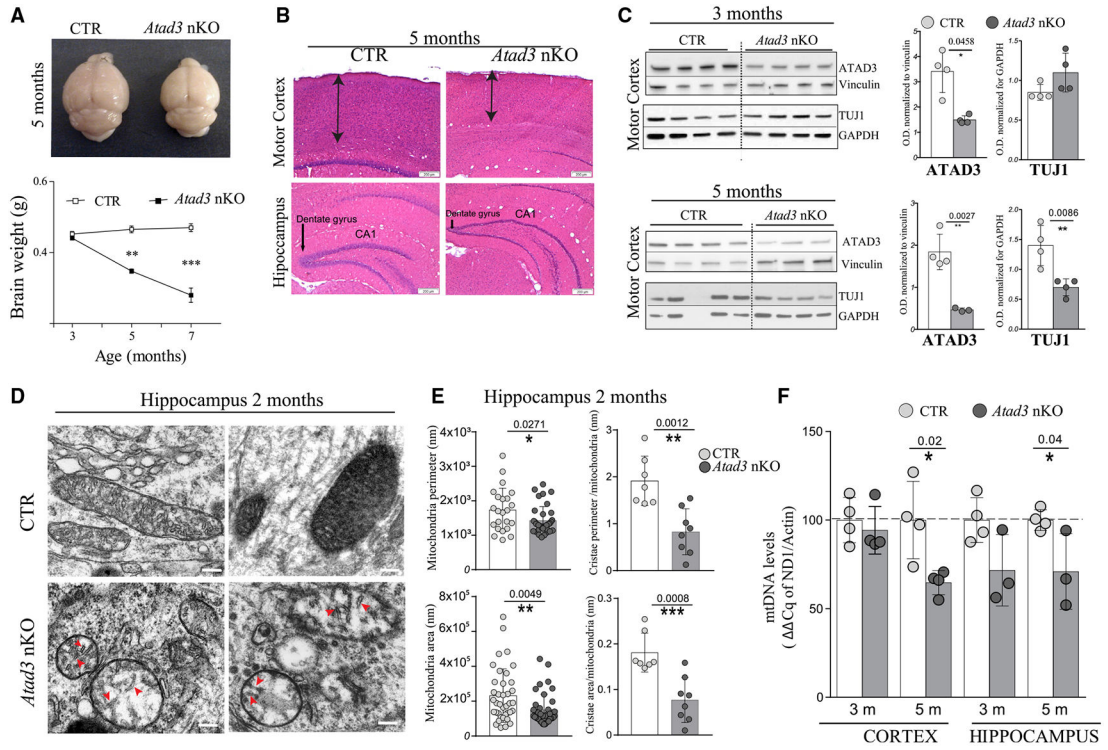
Figure 2. Loss of ATAD3 in brain disrupts mitochondrial cristae structure and causes neurodegeneration

(A) Brain weight *Atad3* nKO and control (CTR) mice of 3, 5, and 7-month-old male mice (n = 4–6) showing reduced size from 5 months old.

(B) H&E staining of cortical (first row) and hippocampal (second row) regions of 5-month-old animals (arrows show neuronal loss). Original magnification × 10.

(C) Western blots and relative quantifications of ATAD3 and the neuronal marker TUJ1 in homogenates from motor cortex of 3- and 5-month-old mice. Data are represented as mean ± SD (n 3/group). *P*-values were determined by *Student's t test*. **p < 0.01, ***p < 0.001.

(D) Representative electron-dense transmission micrographs (TEM) of mitochondria from CA1 hippocampus region of 2 months old control (CTR) and *Atad3* nKO mice. Condensed cristae (red arrowheads) and smaller diameters are shown (scale bar, 200nm).

(E) Quantification of the mitochondrial perimeter, area, and cristae surface (expressed as cristae perimeter per mitochondrial perimeter or area, respectively). Data represent mean ± SD of n = 3 different sections (> 20-30 mitochondria) of two control and *Atad3* nKO mice. *P*-values were calculated by *Student's t test* to determine the level of statistical difference; *p < 0.05, **p < 0.01 and ***p < 0.0001.

(F) mtDNA levels measured by qPCR in DNA extracted from cortices and hippocampus of 3 and 5-month-old control and *Atad3* nKO mice (n = 4–5/group). Bars represent means ± SD). p values were calculated by *Student's t test* to determine the level of statistical difference; *p < 0.05, **p < 0.01 and ***p < 0.0001.
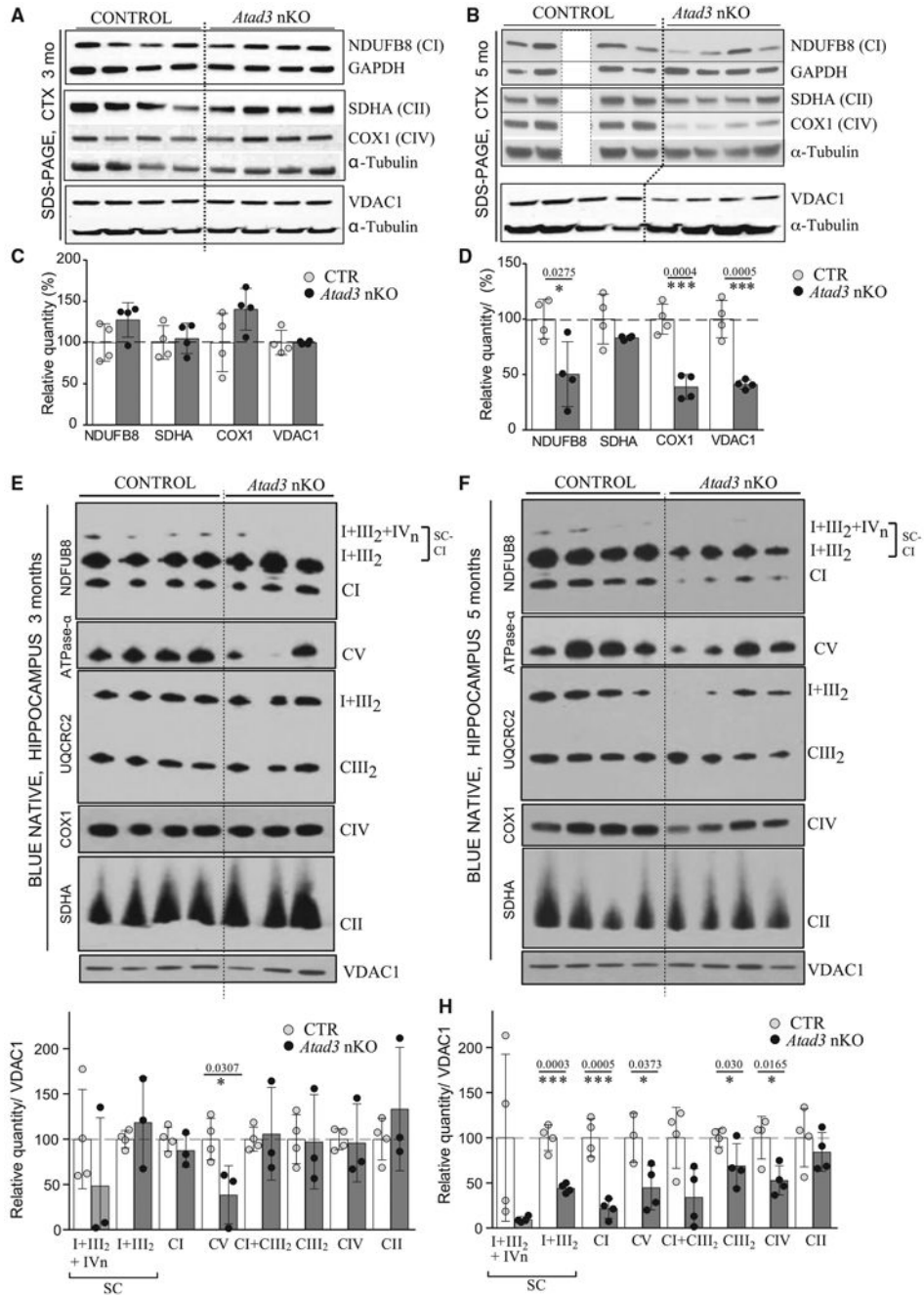
Figure 3. Analysis of the OXPHOS subunits and OXPHOS complex steady-state levels in *Atad3* nKO brain

(A and B) western blots probing mitochondrial oxidative phosphorylation complex subunits (NDUFB8, SDHA and COX1) and VDAC1 in cortex homogenates from control and *Atad3* nKO at 3 and 5 months of age.

(C and D) Quantifications for of the western blots showed in A and B, respectively.

(E) Blue Native PAGE blots probing mitochondrial oxidative phosphorylation complexes and supercomplexes in hippocampal homogenates from control and *Atad3* nKO at 3 months of age and (G) relative quantifications. (F) BN-PAGE blots probing mitochondrial oxidative
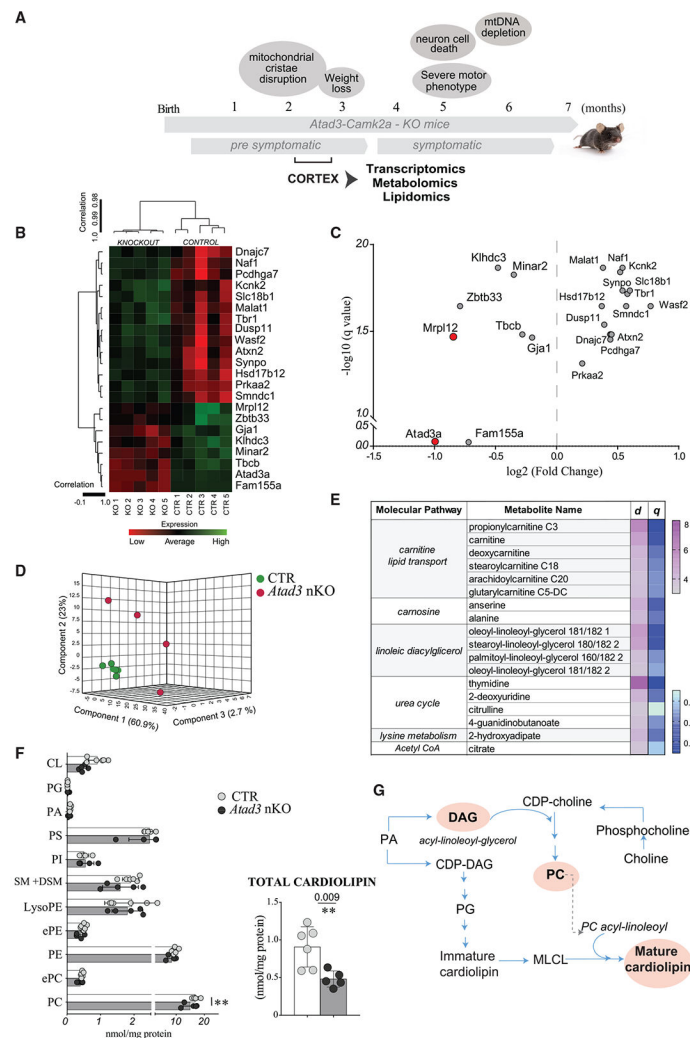
phosphorylation complexes and supercomplexes in hippocampal homogenates from control and *Atad3* nKO at 5 months of age and (H) relative quantifications. Bars represent means ± SD. p values were calculated by *Student's t test* to determine the level of statistical difference; $*p < 0.05$, $**p < 0.01$ and $***p < 0.0001$.

Figure 4. Multi-omics analysis in pre-symptomatic *Atad3* nKO brain

(A) Schematic representation of the phenotype found in the ATAD3A nKO mouse model. Cortex tissue samples were used for the Multi-omics analysis which included transcriptomics, metabolomics, and lipidomics at 2.5-month-old between control (CTR) and *Atad3* nKO mice. (B and C) Transcriptomic analysis.

(B) Supervised hierarchical clustering heatmap representation of the 22 differentially expressed genes by DESq2 between control CTR and Atad3 nKO mice (n = 5 per group). Green color indicates overexpression and red indicates under-expression.

(C) Volcano plot of the 22 differential expressed genes. Top under-expressed transcripts included Atad3a and Mrpl12 (shown in red). Data are expressed as $\log_2$ fold change with adjusted p value (Benjamini-Hochberg adjusted, q-value < 0.05).

(D and E) Metabolomics analysis.

(D) 3D Partial Least-Squares Discriminant Analysis (PLS-DA) score plot showing the separation between CTR (n = 6) and Atad3 nKO mice (n = 4). Explained variables are shown in parenthesis for the 3 principal components.

(E) SAM (Significance Analysis of Microarrays) table showing 27 significant overexpressed metabolites grouped by common functional pathway. Cutoff significance (d value = 1.4), FDR (q value) = 0.043.

(F) Lipidomics analysis. Lipid content levels of the major phospholipid species detected showing a decrease of total PC (phosphatidylcholine) in the Atad3 nKO group (2way ANOVA p = 0.012). Independent analysis of the total Cardiolipin content also show a decrease in nKO mice group (n = 6 mice per group). *p < 0.05, **p < 0.01 and ***p < 0.0001. PG (phosphatidylglycerol), PA (phosphatidic acid), PS (phosphatidylserine), PI (phosphatidylinositol), ePE (ether-linked phosphatidylethanolamine), PE (phosphatidylethanolamine), lysoPE (lysophosphatidylethanolamine), ePC (ether-linked phosphatidylcholine), SM (sphingomyelin), DSM (dihydrosphingomyelin), cardiolipin (CL).

(G) Phospholipid synthesis Pathway identified in our Integrated Omics analysis. DAG (diacylglycerol) and linoleic acylglycerols are preferentially used in two different reactions during the synthesis of phospholipids, integral components of mitochondrial membranes: 1. DAG is converted to cytidine diphosphate-diacylglycerol (CDP-DAG) by a cytidylyltransferase enzyme using PA located in the ER. CDP-DAG is then used as substrate through PG for the synthesis of CL. 2. DAG is also incorporated to the choline moiety of cytidine diphosphate-choline (CDP-choline) during the synthesis of PC. Using the CDP choline pathway, choline (which is located in the ER) follows several enzymatic reactions to form phosphocholine and CDP-choline. Once PC is synthesized in the ER it is translocated to the mitochondria and acts as a major donor of the acyl groups to the immature cardiolipin during the remodeling process within the inner mitochondrial membrane.
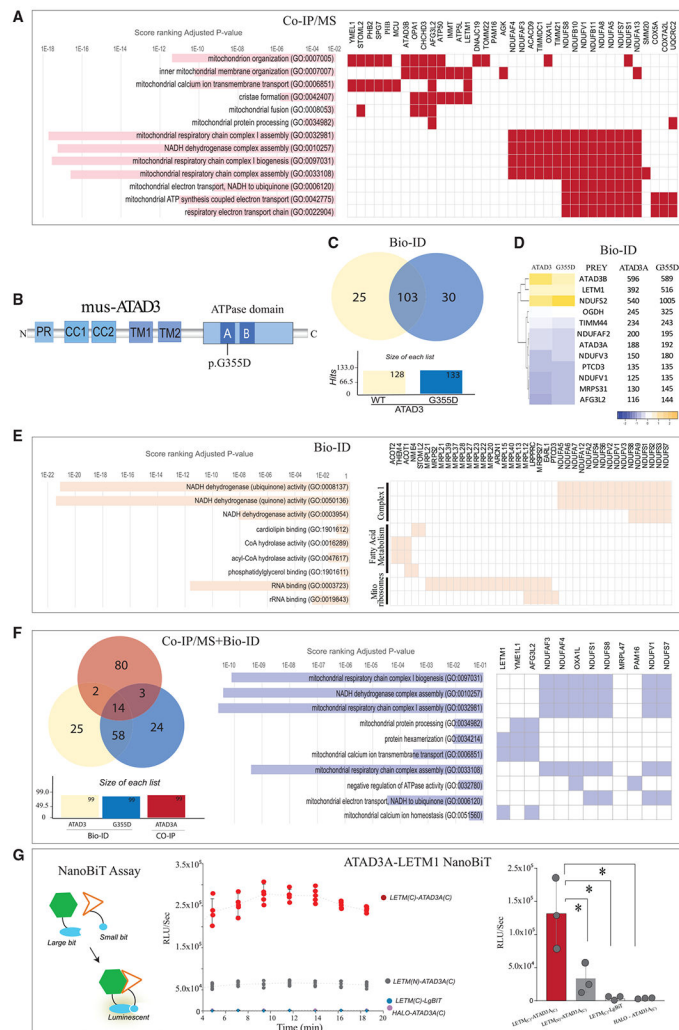
Figure 5. Enrichment and protein interaction analysis of ATAD3A

(A) CoIP analysis. GO enrichment analysis of the first 100 protein hits after co-immunoprecipitation of human ATAD3A showing the list of significant GO terms and annotations by molecular function. Bars represent the adjusted p value and marks on the grid correspond to the proteins annotated by the GO term.

(B) BioID analysis. Representative scheme of the ATAD3 protein and the location of the glycine (G) to aspartate (D) (G355D) in the Walker A motif. The ATPase domain is located at the C-terminal region of the protein and contains the Walker A and the Walker B motif (required for ATP binding and hydrolysis). ATAD3 also contains a proline-rich domain (PR) at the N-terminal tail followed by two coil-coil domains (CC1 and CC2) and 2 transmembrane domains (TM1 and TM2).

(C) Venn diagram of the common hit proteins found by BioID for the wild-type (ATAD3) and mutant (G355D) baits. 103 common preys were found between both groups while 25 unique preys were found in the ATAD3 and 30 in the G355D.

(D) Hierarchical clustering of the common 12 top significant preys detected in both (ATAD3) and (G355D) with a BFDR < 0.01. The fold change score (calculated over the average of 23 controls) is shown for each bait.

(E) Enrichment analysis of the common 103 preys found in BioID analysis. Top GO terms listed by molecular function are shown in bars representing the combined adjusted score ranking. GO terms are grouped in three distinctive pathways, complex I, mitoribosomes, and fatty acid metabolism. Protein members belonging to each term are shown in color on the grid of squares.

(F) CoIP/MS+BioID. (left panel) Venn diagram showing the overlapping significant genes between the first 100 top hits found by coIP (ATAD3) and BioID wild-type and mutant G355D. (*right panel*). Enrichment analysis by Biological process of the common 14 proteins found between coIP and BioID analysis. The top 10 GO terms are shown in bars representing the combined adjusted score ranking and proteins belonging to each term are shown in color on the grid of squares.

(G) LETM1 interacts with ATAD3A. (*left panel*) schematic representation of the NanoBit Assay. The Nanoluc luciferase relies on the structural complementation of two split subunits: small Bit and large Bit. These subunits act as a reporter and are fused to the N or C-terminal region of the two proteins of interest, which upon interaction form the active enzyme able to generate bioluminescence. (*central panel*) Kinetic *in vivo* luminescence data of the different pair combinations of LETM1 and ATAD3A fused to the subunits of the NanoLuc luciferase. Complementation was tested fusing the reporters at the C-terminal ATAD3A$_{(C)}$ and both terminal regions of the LETM1 protein, LETM1 C-terminal (LETM1$_{(C)}$ shown in red) or LETM1 N-terminal LETM1$_{(N)}$ shown in gray). LgBiT (Large Bit) and SmBit (HALO Small Bit) fragments were used as nonspecific complementation interactions at the C-terminal and N-terminal regions, respectively. The graph shows the relative luminescence units per second (RLUs/sec) over time (in minutes). (*right panel*) Luminescent signal was significant among the C-terminal of LETM1 and ATAD3A when compared to nonspecific interaction controls (LETM$_{(C)}$-LgBiT $p = 0.015$ HALO-ATAD3A$_{(C)}$ $p = 0.015$) or the LETM$_{(N)}$-ATAD3A$_{(C)}$ $p = 0.044$) values were calculated by *Student's t test* to determine the level of statistical difference; *$p < 0.05$, **$p < 0.01$, and ***$p < 0.0001$. 3 independent experiments (4 technical replicates each)
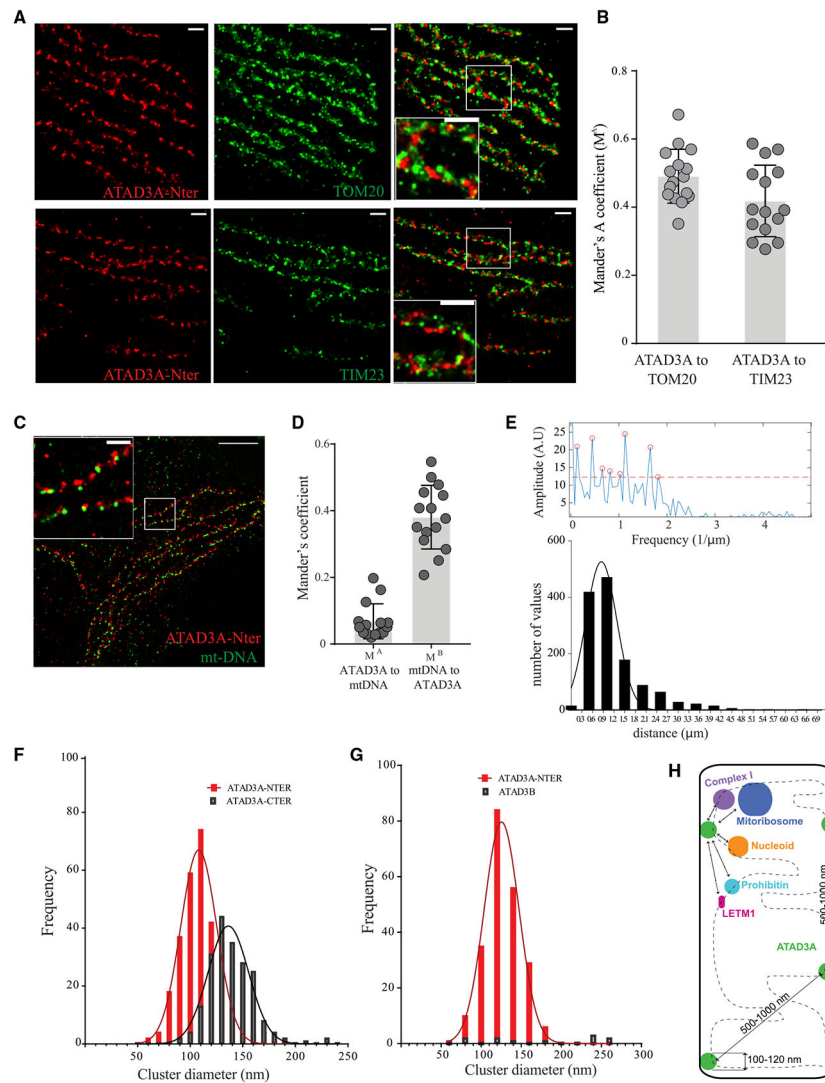
Figure 6. Super resolution analysis of the spatial distribution of ATAD3A in HeLa cells

(A) HeLa cells labeled with ATAD3A (N-terminal antibody) (red) and TOM20 as an outer mitochondrial membrane marker (green upper panel) or TIM23 as the inner mitochondrial membrane marker (green lower panel) were analyzed by STORM.

(B) Co-localization expressed as Mander's coefficient showing the co-occurrence measurements (Manders A) of ATAD3A with TOM20 and with TIM23, respectively (n = 16 cells each).

(C) Overlay STORM reconstructed image of ATAD3A N-terminal antibody (ATA3A-Nter) staining (red) and anti-mtDNA (mtDNA) in green. (Scale bar, 5 μm; inset scale bar, 1 μm).

(D) Co-occurrence Manders coefficients of ATAD3 signal co-localizing with mtDNA (Manders A) and mtDNA co-localizing with ATAD3A (Manders B). (n = 16 cells) (E). (upper panel): Representative graph of the intensity profile after Fast Fourier Transform of ATAD3A N-terminal SMLM showing the peak detection amplitude as a function of the inverse of the distance (1/μm). Peaks that exceed the amplitude threshold are shown in red circles and were used for distribution analysis. (amplitude threshold is denoted by the red

dot-line and represents 50% of the maximal amplitude detected in the intensity profile). (Lower panel): Histogram showing the distribution of ATAD3A periodicities by ranges (bins of 0.5 μm). The most frequent ATAD3A periodic signal was detected at 0.5 and 1 μm. Nonlinear regression with Gaussian fit is shown in black (Amplitude:526.3; mean:0.8461; SD:0.4339). Total number of periods detected by FFT above the amplitude threshold were used from n = 12 cells (560 intensity profile tracings, 1313 periodic values).

(F–G) Histogram showing the distribution of the ATAD3 cluster diameters found by SR Tessler analysis. (F) ATAD3A N-terminal (red) and C-terminal (black) shows clusters with a diameter of 110.7 nm (Best-fit values: Amplitude:66.96, Mean:108.1, SD:17.16) and 139 nm (Best-fit values: Amplitude: 40.72, Mean: 136.3, SD 19.31), respectively. (G) Frequency distribution cluster at the ATAD3A N-terminal (in red) and absence of organized clusters with the ATAD3B (in black). Nonlinear regression with Gaussian fit is shown on each frequency distribution plot. Datasets correspond to n = 9 cells from three independent single-molecule experiments. Statistics were performed on the dataset computed from the Voronoï diagram on detected localizations and normalized by the average localization density.

(H) Schematic model of the ATAD3 submitochondrial localization and scaffold function. ATAD3A spans the outer and inner mitochondrial membrane forming oligomeric clusters of approximately 100 to 120 nm on both N and C-terminal, respectively. The protein is distributed regularly each 500 to 1000nm along the mitochondrial membranes. We propose ATAD3A acts as a scaffold, perhaps distributing and arranging different protein complexes within mitochondrial membranes or sub-compartments in an ATPase-dependent manner

KEY RESOURCES TABLE

Reagent or resource	Source	Identifier
Antibodies		
ATAD3 N-terminal Rabbit polyclonal	Proteintech	C#16610-1-AP
ATAD3 C-terminal Mouse monoclonal	Santacruz	C# 376185
ATAD3B(A-8) Mouse monoclonal	Santacruz	C#514615
TOM20 (F-10) Mouse monoclonal	Santacruz	C#17764
TOM20 Rabbit polyclonal	Sigma-Aldrich	C#HPA011562
TIM23 Mouse monoclonal	BD Biosciences	C# 611222
ANTI-DNA Mouse monoclonal	CBL186-EMD	C# CBL186-EMD
Anti-rabbit Rabbit polyclonal	Novus biologicals	C# NBP1-72732JF646
Anti-mouse Mouse polyclonal	Thermo-Fisher	C# A-11004
ATAD3-N-terminal	Abcam	C#188386
IgG- Rabbit polyclonal	Millipore	C#12-370
Anti-NanoLuc® Monoclonal Antibody	Promega	C# N7000
Anti-ATAD3 rabbit pre-immune Serum 3	GenScript	C#SC1088
Anti-NDUFB8	Abcam	C#ab110242
Anti-SDHA	Abcam	C#ab14715
Anti-COX1(Anti-MTCO1)	Abcam	C#14705
Anti-UQCRC2	Abcam	C#203832
Anti-ATPase-α	Abcam	C#14748
Anti-VDAC1/Porin	Abcam	C#14734
Anti-Tubulin	Milipore-Sigma	C#T9026
Anti-β Actin	Milipore-Sigma	C#A2066
Anti-TUJ1	Covance	C# MMS-435P
Anti-GAPDH	Ambion	C#4300
Anti-Vinculin	AbCam	C#Ab130007
Bacterial and Virus Strains		
StellarTM competent Cells	TAKARA	C#636763
Critical Commercial Assays		
QuikChange XL site-Directed Mutagenesis kit	Agilent technologies	C#200521
NanoBiT® PPI Starter System	Promega	C#N2015
Deposited Data		
Tafazzin mutant samples	Van Strien et al., 2019	Table S3
Neonate brain samples	Stepanova et al., 2019	Table S1
RNA sequencing	Illumina NovaSeq 6000	GEO (GSE186409)
Metabolomics	Metabolon	Metaboligth (MTBLS3786)
Experimental Models: Cell Lines		
HEK293T	ATCC	C# CRL-1573
HELA	ATCC	C# CCL-2
Flp-In T-REx 293	Invitrogen	Cat# R78007

Reagent or resource	Source	Identifier
Experimental Models: Organisms/Strains		
Mouse: *CaMK-IIα Cre*	Dragatsis and Zeitlin, 2000	N/A
Mouse: *Atad3-CaMK-IIα* KO. *Atad3* neuronal specific knockout.	This paper	This paper
Mouse: *Atad3* *(LoxP/LoxP)*.	Peralta et al., 2018; PMID:29898916. Developed by Carlos T. Moraes lab.Figure S1	MGI, catalog # 6197947
Oligonucleotides		
F- MUT-1059-GAC	IDT	5′cgggccacctgacacagggaagac-3′
R- MUT-1059- GAC	IDT	5′-gtcttccctgtgtcaggtggcccg-3′
mtDNA ND1-F	IDT	5′-CAGCCTGACCCATAGCCATA-3′
mtDNA ND1-B	IDT	5′-ATTCTCCTTCTGTCAGGTCGAA-3′
β-actin-F	IDT	5′-GCGCAAGTACTCTGTGTGGA-3′
β-actin-B	IDT	5′-CATCGTACTCCTGCTTGCTG-3′
Recombinant DNA		
pcDNA5-pDEST-BirA-Flag C-terminal	Antonicka Lab	N/A
pFN35K SmBiT-LETM1-TK-neoFlexi®	this study	N/A
pFC36K SmBiT-LETM1-TK-neoFlexi® Vector	this study	N/A
pFC34K LgBiT-ATAD3a- TK-neoFlexi® Vector	this study	N/A
SmBiT-PRKACA	Promega	N2015
LgBiT-PRKAR2A	Promega	N2015
NanoBiT® Halo tag	Promega	N2015
pcDNA5-pDEST-hATAD3A-BirA-Flag C-terminal	This study	N/A
pcDNA5-pDEST-hATAD3A-G355D-BirA-Flag C-terminal	This study	N/A
Software and Algorithms		
BaseSpace®	Illumina	https://login.illumina.com/
Metaboloanalyst		https://www.metaboanalyst.ca
Enrichr	Kuleshov et al., 2016	https://maayanlab.cloud/Enrichr/
DAVID Bioinformatics Resources 6.8		https://david.ncifcrf.gov/
Jvenn diagrams	Bardou et al., 2014	http://jvenn.toulouse.inra.fr/app/index.html
ImageJ		https://imagej.nih.gov/ij/
MATLAB		https://www.mathworks.com/
Thunderstorm (1.3-2014-11-08)	Ovesný et al., 2014	https://zitmen.github.io/thunderstorm/
Coloc-Tesseler software	Levet et al., 2019	https://github.com/flevet/Coloc-Tesseler
GraphPad Prism 7		https://www.graphpad.com
SR-Tesseler version 1.0.0.1	Levet et al., 2015	https://github.com/flevet/SR-Tesseler
CF-MS meta-analysis	https://fosterlab.github.io/CF-MS-analysis/	https://cf-ms-browser.msl.ubc.ca/
Image lab 6.1.0	Bio-Rad	https://www.bio-rad.com